Unterschrift Betreuer

TU WIEN

**TECHNISCHE
UNIVERSITÄT
WIEN**
Vienna University of Technology

DIPLOMARBEIT

Comparison of Advanced Treatment Techniques
for Lung Cancer

Ausgeführt am Atominstitut
der Technischen Universität Wien

unter der Anleitung von
Univ.Prof. Univ.Lektor Dr. DI Dietmar Georg
und **DI Wolfgang Lechner, PhD**
als verantwortlich mitwirkenden Universitätsassistenten

durch **Marie-Theres Bsteh, BSc**
Schenkendorfgasse 43/28, 1210 Wien

20.Oktober 2016   Unterschrift Student

Danksagung

Zu Beginn möchte ich mich bei Univ.Prof. Univ.Lektor Dr. DI Dietmar Georg bedanken. Danke, dass Sie mir diese Arbeit an der Universitätsklinik für Radiologie am AKH Wien ermöglicht haben.

Im weiteren möchte ich mich beim gesamten Radonc Team für die ständige Hilfsbereitschaft bedanken. Aber vor allem bei DI Wolfgang Lechner, PhD, für die Ideen, das produktive Feedback und die Geduld: Vielen Dank für deine Hilfe!

Ich möchte mich auch bei meiner Familie, meinen Freunden und Studienkollegen für die Unterstüzung während meiner Studienzeit bedanken.
Besonders möchte ich mich an dieser Stelle bei meinen Eltern bedanken. Danke, dass ihr mir meine Ausbildung ermöglicht und mich bei allem unterstützt habt. Vielen Dank auch für eure Geduld und euer Verständins.

Weiters möchte ich mich bei Lexi für das sprachliche Feedback bedanken. Danke für deine hilfreichen Englisch-Tipps und die immer wieder motivierenden und aufbauenden Worte.

Ganz besonders möchte ich mich noch bei meinem Freund bedanken. Fabian, vielen Dank für deine unglaubliche und unersetzbare Unterstützung, dein Verständnis und deine ständig positiven Worte. Danke, dass du mein häufiges Gesuder und meinen Vogel in den letzen Monaten ertragen und mich immer wieder motiviert hast!

Abstract

This thesis discusses a variety of treatment methods for lung cancer using flattened and unflattened photon beams. Therefore, treatment plans for volumetric modulated arc therapy (VMAT) and dynamic conformal arc therapy (DCAT) using flattened and unflattened photon beams were generated using the treatment planning system Monaco 5.00.04 (Elekta AB, Stockholm, Sweden). For every treatment method two different dose prescriptions, following an in-house stereotactic body radiation therapy (SBRT) protocol as well as recommendations according to the ICRU 83 report, were applied.
All plans were generated for ten different patients recently treated at the Medical University of Vienna as well as for an in-house developed breathing phantom and were compared to the clinically used unflattened 3D conformal radiation therapy (3D-CRT) plans which were generated with the treatment planning system Oncentra (Elekta AB, Stockholm, Sweden).

For four patients with the tumor in the left lung and for the phantom itself, all plans were irradiated to the breathing phantom. Thereby, it was possible to determine the influence of the interplay between target motion and the leaf-motion of the multi-leaf-collimator and the thereby induced change of the target dose. The in-house developed breathing phantom used for this study, called ARDOS, consists of tissue-equivalent solid water, bone equivalent tissue (to simulate the ribs) and lung-equivalent high density balsa wood. This phantom enables the simulation of chest motion, rib motion as well as longitudinal and rotational tumor motion. For the determination of the interplay effect, the plans were irradiated to the phantom without phantom motion, with longitudinal tumor motion and with a combination of longitudinal and rotational tumor motion.

Due to their high spatial resolution in two dimensions radiochromic films, in detail GAFChromic EBT3 films (Ashland ISP, Wayne, NJ), were used. These films provided an optical dose range of 0.2 to 10 Gy and a dynamic dose range of up to 20 Gy.

Evaluation of the treatment plans showed that the SBRT VMAT plans provided best dose conformity and organ at risk sparing, compared to the other plans. In contrast, due to the higher prescribed doses, all ICRU plans exhibited a worse dose conformity and higher doses to the organs at risk. The comparison also showed that no significant

differences concerning dose coverage, dose conformity and dose to the organs at risk occurred for flattened and unflattened treatment plans. The main difference was the substantial reduced beam-on time for unflattened treatment plans. Furthermore, the beam-on time was reduced by the use of 3D-CRT treatment plans compared to VMAT plans which was caused by the highly significant increase of monitor units for VMAT plans.

The measurements showed that for the used dose range of 15-27 Gy the use of the green channel led to a more accurate dose determination than the red channel.
The evaluation of the interplay effect on realistic tumor motion and no tumor motion showed the lowest influence on the mean dose of 2-3 % for 3D-CRT and DCAT plans, with the 3D-CRT exhibiting a reduction of the mean dose to the target and the DCAT plans an respective increase. In contrast to that, VMAT plans showed an increase of the mean dose by 5-7 % due to the interplay effect. However, it has to be mentioned that the uncertainty of measurement was estimated to be approximately 5 % due to the use of the films at the limits of their dose range.

Since the improvements of treatment plan quality of SBRT VMAT plans were not significant, the SBRT 3D-CRT plans provide the optimal type of therapy due to the shortest beam-on time and the lowest influence of the interplay effect.

Kurzzusammenfassung

Diese Arbeit diskutiert verschiedene Bestrahlungsmethoden für Lungentumore unter der Verwendung von Photonenstrahlen mit und ohne Ausgleichsfilter (FF und FFF). Dafür wurden Bestrahlungspläne für volumenmodultiere Strahlentherapie (VMAT) und dynamisch konforme Strahlentherapie (DCAT) für FF und FFF Photonenstrahlen mittels dem Monaco 5.00.04 (Elekta AB, Stockholm, Sweden) Planungssystem generiert. Zusätzlich wurden für jede Bestrahlungsmethode zwei verschiedene Dosisverschreibungen, folgend einem internen Protokoll für stereotaktische Strahlentherapie am Körper (SBRT) und den Empfehlung des ICRU 83 Reports, verwendet.
Alle Pläne wurden für zehn verschiedene Patienten, welche kürzlich an der Medizinischen Universität Wien behandelt wurden, und für ein intern entwickeltes Atmungsphantom generiert und mit den klinisch verwendeten 3D konformalen Strahlentherapieplänen (im FF-Modus), welche mit dem Oncetra (Elekta AB, Stockholm, Sweden) Planungssystem generiert wurden, verglichen.

Für vier Patienten, mit dem Tumor in der linken Lunge, und für das Phantom selbst, wurden alle Pläne auf das Atmungsphantom abgestrahlt. Das intern entwickelte Atmungsphantom, genannt ARDOS, besteht aus gewebeäquivalentem festem Wasser, knochenäquivalentem Gewebe (für die Simulation der Rippen) und lungeäquivalentem Balsaholz hoher Dichte. Dieses Phantom ermöglicht die Simulation von Brustkorbbewegung, Rippenbewegung und longitudinaler und rotierender Tumorbewegung. Dadurch war es möglich den Interplay-Effekt zwischen der Tumorbewegung und der Lamellenbewegung des Multilammelenkollimators und die dadurch verursachte Änderung der Tumordosis zu untersuchen. Dafür wurden die Pläne auf das Phantom ohne Bewegung, mit longitudinaler Tumorbewegung und mit einer Kombination aus longitudinaler und rotierender Tumorbewegung abgestrahlt.

Aufgrund der hohen räumlichen Auflösung in zwei Dimensionen wurden Radichrom-Filme, im speziellen GAFChromic EBT3 Filme (Ashland ISP, Wayne, NJ), verwendet. Diese Filme haben einen optimalen Dosisbereich von 0,2 bis 10 Gy und einen dynamischen Dosisbereich bis zu 20 Gy.

Die Evaluierung der Bestrahlungspläne zeigte, dass SBRT VMAT Pläne die beste Konformität der Dosis ermöglichen und die Risikoorgane bestmögliche aussparen, im Gegen-

satz zu den andern Plänen. Im Vergleich dazu wiesen alle ICRU Pläne eine schlechtere Konformität der Dosis und eine höhere Dosis der Risikoorgane auf, verursacht durch die höhere verschriebene Dosis. Zusätzlich zeigte der Vergleich, dass keine signifikanten Unterschiede bezüglich der Dosis Abdeckung, Konformität und Dosis der Risikoorgane zwischen FF und FFF Bestrahlungsplänen auftreten. Der hauptsächliche Unterschied war die wesentliche Verringerung der beam-on Zeit für FFF Pläne. Zusätzlich konnte die beam-on Zeit durch die Verwendung der 3D-CRT Bestrahlungspläne statt der VMAT Pläne, aufgrund der sehr signifikanten Erhöhung der Monitor Einheiten für VMAT Pläne, reduziert werden.

Die Messungen haben gezeigt, dass für den verwendeten Dosisbereich von 15-17 Gy, der grüne Kanal genauere Ergebnisse für die Bestimmung der Dosis lieferte als der rote Kanal.
Die Evaluierung des Interplay-Effekts für realistische Tumorbewegung und keine Tumorbewegung zeigte den kleinsten Einfluss des Effekts auf die mittleren Dosis von 2-3% für 3D-CRT und DCAT Pläne. Während die Dosis der 3D-CRT reduziert wurde, wurde die Dosis der DCAT Pläne erhöht. Im Vergleich dazu zeigten die VMAT Pläne eine Erhöhung der mittleren Dosis von 5-7 % aufgrund des Interplay-Effekts. Jedoch muss erwähnt werden, dass aufgrund der Verwendung der Filme am Limit des Dosisbereichs, die Messunsicherheit auf etwa 5 % geschätzt wurde.

Da die SBRT VMAT Pläne keine signifikante Verbesserung der Bestrahlungsqualität ermöglichen, bieten die SBRT 3D-CRT Pläne optimale Therapie aufgrund der kürzesten beam-on Zeit und des geringsten Einflusses des Interplay-Effekts.

Contents

1 | Introduction

In the year 2012, 3673 people in Austria died from lung cancer [60] and 4573 were diagnosed to suffer from lung cancer [59]. For men, lung cancer is the most common form of cancer, considering death cases caused by cancer. For women, it is still the second most common cause of death. It is thus evident that there is still the need to improve lung cancer therapy.

One important method for lung cancer therapy is radiation therapy. This kind of therapy uses high-energy radiation for cancer treatment. Therefore, accelerated electrons, protons or heavy ions and additionally, photons can be used. The ionizing radiation is directly applied to the tumor tissue (while the surrounded normal tissue is best possible spared) and thereby causes damaging of the DNA or creates free radicals, which also lead to damages of the DNA and thereby destroys the malign tissue. Due to the fact, that, on the one hand, radiation therapy primarily affects cells under cell division and, on the other hand, tumor cells divide faster than other cells, it is possible to destroy tumor cells without destroying healthy cells. Furthermore, healthy cells which are damaged are able to restore faster.

Based on the detectability of the exact tumor tissue, by the use of computer tomography or magnetic resonance tomography, high doses can be applied to the well defined lung tumors. However, lung cancer treatment is challenging due to tumor motion caused by respiration. This respiration motion can bring the tumor out of the irradiation field and thereby reduces the treatment quality. Hence, more irradiation fractions are used (so-called Stereotactic Body Radiation Therapy) to reduce the effects caused by tumor motion. Another challenging task for radiation therapy is the accurate and reproducible positioning of the patients. For accurate positioning markers can be place on the patients, and masks, frames or so-called immobilizations can be used.

Furthermore, there are other cancer treatment methods like surgery, chemotherapy, medication (e.g. hormontherapy) or a combination of these. The choice of the treatment method depends on the tumor's location, the nature of the tumor and the tumor stage.

The tumor is removed by surgery if the tumor has not built metastases and if it is possible to remove the whole tumor without damaging surrounded healthy tissue. In addition to surgery, sometimes radiation therapy or chemotherapy is necessary to pre-

vent the recurrence of the tumor. For chemotherapy pharmaceuticals are used which can be administered orally, intravenously or subcutaneously, thereby damaging cells and preventing the multiplication of the cell. However, chemotherapy can cause many side effects; due to the repeated application of the therapy, the quality of the patient's life is reduced.
For some tumors the growth is dependent on hormones. Hence the prevention of the production of the respective hormone can stop the growth but cannot destroy the tumor [45].

1.1   Physical Background

For photon therapy a high energy photon beam has to be produced out of accelerated electron beams. Therefore, accelerated electrons are shot at a metal target, whereby two different types of photon beams are generated. Electrons with an energy high enough to excite target electrons in the inner shells to higher energy levels can produce so-called characteristic X-rays. Due to the fact that orbital electrons arrange themselves to be in a minimal energy state, another electron will take the initial place of the excited electron. During this process the electron has to lose binding energy, and therefore, emits characteristic X-ray. The following equation describes the process of an atom $A(E_k)$ with an electron in the initial energy level E_k which is excited to $A^*(E_i)$, with the excited electron at the higher energy level E_i [13]

$$
\begin{aligned}
&e^- + E_{kin} + A(E_k) \rightarrow A^*(E_i) + e^- + E'_{kin} \\
&E_{kin} - E'_{kin} = E_i - E_k \\
&A^*(E_i) \rightarrow A(E_k) + h\nu_{ik}
\end{aligned}
\tag{1.1}
$$

If the transition energy from the higher energy level to the lower one is higher than the binding energy of an electron, the electron can be ionized (Auger effect) [6].
The more important effect is created by the generation of photons due to the deceleration of high-energy electrons. Electrons which interact with the target material are either deflected in the Coulomb field of the heavy nucleus, thus emitting their energy through the emission of a continuous photon beam, so-called bremsstrahlung; or the electrons can collide with the target atoms and produce some heat which can then lead to characteristic X-rays due to the excitation of the electrons of the inner shell [13].

The interaction of a photon beam with matter leads to an attenuation of the beam's intensity I_0 due to photon absorption and photon scattering. This decrease in intensity can be described using the linear attenuation coefficient μ which depends on the absorption coefficient α and the attenuation coefficient μ_S [6, 13]:

$$
I(x) = I_0 \, e^{-\mu x}
\tag{1.2}
$$

This attenuation coefficient depends on the energy of the photon ($E = h\nu$) and the atomic number Z of the material [6].

Besides elastic scattering without energy loss (Rayleigh scattering) three other absorption effects occur. One interaction effect, the photo effect, occurs due to the absorption of a photon with an energy smaller than 100 keV and the resulting emission of an electron. Therefore, the energy has to comply with following energy conservation:

$$E_{kin}(e^-) = h\nu - (E_{ion} - E_k) \qquad (1.3)$$

In this relation E_{kin} describes the kinetic energy of the emitted electron, E_{ion} is the ionization energy, and E_k describes the binding energy of the kth shell. Whereas the photon effect describes the absorption of a photon within the electron shell, the nuclear photo effect takes place in the nucleus. For a photon with an energy higher than the binding energy of the nucleons, the absorption of the photon in the nucleus can take place. Thus, a proton or neutron is emitted from the nucleus and a radioactive isotope is created. The energy for the release of a nucleon depends on the atomic number and the atomic mass [38].

Another photon-matter interaction effect is the Compton effect. This effect describes the interaction of a photon with an electron in an outer shell and the resulting partial transfer of energy. Thereby, the scattered photon (hν') loses some energy and can be absorbed through the photo effect. The Compton effect can be described using the following relation:

$$h\nu + e^- \rightarrow e^-(E_{kin}) + h\nu' \qquad (1.4)$$

For photon energies greater than 1 MeV electron-positron pairs can be created [13, 14]:

$$h\nu \rightarrow e^- + e^+ + 2E_{kin} \qquad (1.5)$$

1.2   Biological Background

The application of radiation therapy can be curative but also palliative, in that it can shrink the tumor and improve quality of life. It can be used pre-operative to shrink the tumor and enable removal of the tumor by surgery, intraoperative, or post-operative to prevent repeated occurrence. As already mentioned it can also be used in combination with chemotherapy to damage the tumor cells as much as possible [4, 41, 45, 71].

Concerning radiation therapy two different methods are in use. Firstly, there is brachytherapy for which a radioactive source is directly placed inside the tumor. This source consists of a titanium or stainless steal capsules which are filled with the radioactive nuclide, e.g. ^{137}Cs, ^{192}Ir, ^{60}Co, ^{198}Au and ^{125}I [38]. This treatment method is used for tumors which are reachable via cavities from the outside like the uterus, oesophagus, tracheae, or prostate. Since irradiation starts after the source is positioned, the tumor is irradiated with a high dose while the healthy tissue only receives a low dose. However, only small tumors can be treated by the used of this method.

In contrast to that, the second method, called external beam radiation therapy (EBRT), uses an external beam for irradiation whose source (described in section 1.3 in detail) is positioned further away from the tumor. For this type of therapy, the energy for

the treatment can be delivered by using beams of photons, electrons or hadrons (e.g. protons, neutrons and heavy ions). The aim of EBRT is to irradiate the tumor tissue without irradiating surrounding healthy tissue [45].
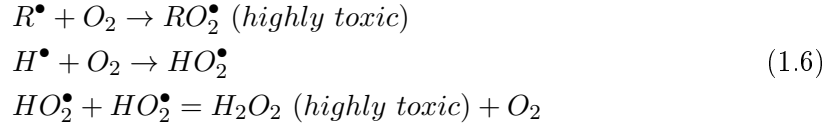
In this study, EBRT is used for cancer treatment.

Radiation therapy causes damages within the irradiated volume, either by direct or indirect action. Direct damages induce ionization and excitation of atoms in the irradiated volume, whereas indirect actions ionize or excite other tissue such as, for example, water molecules, whereby the molecules fall apart and free radicals are produced. Due to the fact that the free radicals are unstable, they interact with neighboring molecules and cause damage [6, 38].

Since indirect damage is predominant in radiation with a low linear energy transfer (LET), it is the main effect for photon beam therapy [6]. The LET is defined as follows:

> " [...] the average energy locally imparted to the absorbing medium by an electron of specified energy in traversing a given distance in the medium."
> (Podgorsak EB, Radiation Oncology Physics: A Handbook for Teachers and Students, 2005, p. 25)

The response of cells to radiation therapy depends on several factors, but predominantly on oxygen. This response develops because free radicals exhibit an unpaired electron which can easily react with the two unpaired electrons of the molecular oxygen. Thus, it leads to an increased probability of DNA damage. Some important examples of increased cell damage caused by oxygen are (R represents an organic molecule and $^\bullet$ represents free radicals) [6]:

$$
\begin{aligned}
R^\bullet + O_2 &\rightarrow RO_2^\bullet \ (highly\ toxic) \\
H^\bullet + O_2 &\rightarrow HO_2^\bullet \\
HO_2^\bullet + HO_2^\bullet &= H_2O_2 \ (highly\ toxic) + O_2
\end{aligned}
\tag{1.6}
$$

The oxygen effect is defined by the oxygen enhancement ratio (OER), which is the ratio of the radiation dose in total absence of oxygen to the dose in the air needed to achieve the same biological effect [38].

The main reason for cell damage due to radiation therapy is DNA damage. DNA is a double-helix molecule which consists of a very long polymer made up of millions of nucleotides. The nucleotides are composed of the nitrogenous bases (adenine, thymine, guanine and cytosine) and a desoxyribose unit which is linked to a phosphorus atom. These bonds between the phosphate and the desoxyribose units keep the DNA together [46]. The bonds can break due to radiation on one side of the double helix (single strand break) or on both sides simultaneously (double strand break). Additionally, base damages can occur due to irradiation [6].

There are multiple mechanisms for detecting and repairing DNA damage. Therefore, multiple irradiation sequences lead to repeated damages of the DNA, potentially at nearly the same location, which then increases the probability of cell death. However, double strand breaks cannot be repaired; in combination with misrepaired damages of

the DNA (mutations or chromosome damage in the cell), they lead to cell death. Instead of dying immediately, most of the cell deaths happen after hours, days or weeks of the treatment. This is caused by the fact that most of the cells undergo cell mitosis and survive until they have to divide [6, 38].

1.3 Particle Accelerators

Particle accelerators are used to increase the kinetic energy of charged particles. In radiation therapy, accelerators are used to generate treatment beams (photon beams, proton beams or beams of heavy ions) at a specific energy level.
Due to the fact that the particles have an energy higher than their rest energy, relativistic formulas have to be used. The following equation describes the relation between the total energy E and the momentum p of a particle:

$$E^2 = E_{kin}^2 + E_0^2 = p^2c^2 + m_0^2c^4 \tag{1.7}$$

In this equation, E_{kin} represents the kinetic energy, while $E_0 = m_0c^2$ describes the rest energy using the rest mass m_0 and c as the speed of light [14]. Dealing with relativistic energies, the mass increase plays an important role.

$$\frac{m(v)}{m_0} = \frac{1}{\sqrt{1 - \frac{v^2}{c^2}}} = \gamma = 1 + \alpha \tag{1.8}$$

$$m(v) = \gamma \cdot m_0 = \frac{m_0}{\sqrt{1 - \frac{v^2}{c^2}}} \tag{1.9}$$

$$\mathbf{p} = m(v) \cdot \mathbf{v} = m\mathbf{v}(1 + \alpha) \tag{1.10}$$

$$\alpha = \frac{E_{kin}}{m_0c^2} \tag{1.11}$$

Equation 1.9 describes the increase of the mass depending on the speed of the particle. For a speed of $0.99\,c$ the mass equals around 7 times the rest mass m_0 [12].
For particles (especially for electrons) which have a kinetic energy higher than two times the rest energy, $E_{kin} > 2m_0c^2$, the increase of the momentum with increasing α is caused by an increase of the mass due to their nearly constant velocity [14].

There are two kinds of particle accelerators. First, there are electrostatic or direct accelerators which are constructed using an evacuated tube in which the particles (electrons or positive ions, mostly protons or D^+) are accelerated. In this tube the particles are accelerated from the cathode with a negative or positive potential (depending on the particle) to the anode which is at ground potential. The kinetic energy of the accelerated particle depends on the charge of the particle q and the applied voltage U between the electrodes (E_{kin} = q·U). One example of an electrostatic accelerator is the Van de Graaff accelerator which is composed of a ribbon generator and an acceleration

tube. This generator enables energy delivery of 5,1 MeV to electrons [2, 14].

Second, there are periodic accelerators. An example of a historically important periodic accelerator is the betatron, a common accelerator for radiation therapy using electrons. It can be used for the acceleration of electrons up to 10^7 eV and is nowadays replaced by accelerators which enable the acceleration to higher energies.

The betatron consists of a magnet yoke, two toroidal induction coils and a vacuum tube in which the electron beam is accelerated (figure 1.1). A magnetic field, which changes with time, induces an electrical field corresponding to Maxwell's induction law:

$$\mathbf{rotE} = -\frac{d\mathbf{B}}{dt} \tag{1.12}$$

The circular force lines of the electrical field are oriented in such a way that the electrons are accelerated. Additionally, the magnetic field holds the electrons on the circular path. To do that the magnetic field has to comply with the so-called Wideroe- or betatron-constraint

$$B(r_0) = \frac{1}{2} \cdot \langle B \rangle \tag{1.13}$$

which demands that the magnetic field at the orbit has to be equal to half the average of the magnetic field within the orbit [2, 14].
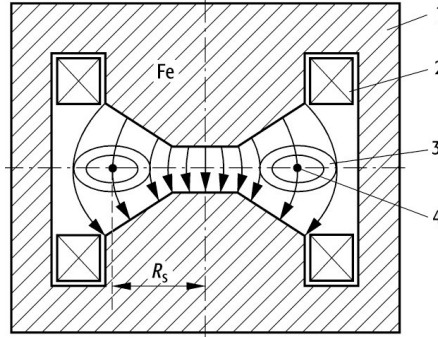

Figure 1.1: Profile of a betatron. 1: magnet yoke, 2: coil, 3: vacuum tube, 4: electron beam [58]

Another type of accelerator which accelerates particles to very high energies is a synchrotron. Since the energy achieved by using a betatron or a cyclotron is limited due to the proportional increase of the accelerator's radius depending on the relation of E_{kin}/B, the accelerators would get very large. To avoid this a synchrotron uses a high-frequency electrical alternating field for the acceleration of the particles. Therefor the synchrotron exists of a toroidal vacuum tube, which is surrounded by a C-shaped magnet yoke and field coils to force the particles to follow a circular path. For the acceleration cavity resonators are used. Due to the increase of the radius with the momentum, the magnetic field hast to be increased to hold the particles on the circular path [2, 14]:

$$|q|vB = \frac{mv^2}{r} \rightarrow r = \frac{p}{|q|B} \tag{1.14}$$

Different magnets are used in combination with synchrotrons. Dipole magnets are used to change the particle's trajectory; quadrupol- and sextupolmagnets for beam focusing; kicker magnets to guide the beam out of the accelerator; and wiggler magnets for the production of synchrotron radiation [2].

In the context of radiation therapy, the linear accelerator (LINAC) is the most important form of accelerator. It uses electrical alternating fields but, in contrast to the synchrotron, the particles are accelerated along a linear path. One type of linear accelerator is the drift tube LINAC (discontinuous accelerator) which can be used for the acceleration of protons and heavy ions. The particles drift along a row of field free cylindrical electrodes (drift tubes) between which a high frequency field accelerates the particles. Due to the fact that the particle's energy increases and thereby the particles move faster, the drift tube's length (L) has to increase so that the oscillation field accelerates the particle with the same polarity [2, 14]. To accelerate the particles using the right polarity, half of the high frequency period ($\frac{T}{2}$) has to be equal to the time of flight Δt [14]:

$$\frac{T}{2} = \Delta t = \frac{L}{v} \rightarrow L = v \cdot \frac{T}{2} \tag{1.15}$$

Since electrons reach the speed of light very fast, the increase of energy is caused by an increase of mass. Therefore, the drift tube LINAC cannot be used for the acceleration of electrons; otherwise the tubes would have to be very long. Hence, traveling wave (continuous) linear accelerators are used for the acceleration of electrons. For this, an electromagnetic wave travels through a "loaded waveguide" (cylindrical waveguide with perforated discs, figure 1.2(a)). For the propagation of a traveling wave, the electrical field has to have a z-component in the direction of propagation with the same sign as the electron which has to be accelerated [2]. From this follows that the phase velocity of the electron and the wave have to be almost equal. This can be achieved through the adaption of the relation of the aperture diameter to tube diameter (2a/2b in figure 1.2(a)). Due to the movement of the electron with the traveling wave, the electron gains kinetic energy. At the same time, at the end of the tube the electron leaves the tube divided in packages with almost speed of light [2, 14].

Other principles for the acceleration of electrons are standing wave accelerators. They are constructed so that the electromagnetic wave is reflected at the end of the tube. Thus, a standing wave is built which enables acceleration of the electrons. Due to the fact that not every cavity carries an electric field, the electrons are accelerated by an antinode. After this, the electrons move with constant velocity within a cavity. After passing the cavity, the standing wave has changed and offers another positive maximum for the acceleration of the electrons [2].

A medical linear accelerator consists of various components, as shown in figure 1.2(b). The first part of a medical accelerator is the electron gun, consisting of a heated cathode and a grounded anode. Due to the cathode's heat, electrons are emitted, accelerated to the anode, and injected into the accelerating waveguide. The electrostatic field which accelerates the emitted electrons is supplied from the pulsed modulator to the cathode. For further acceleration in the accelerating waveguide, microwaves are produced by the

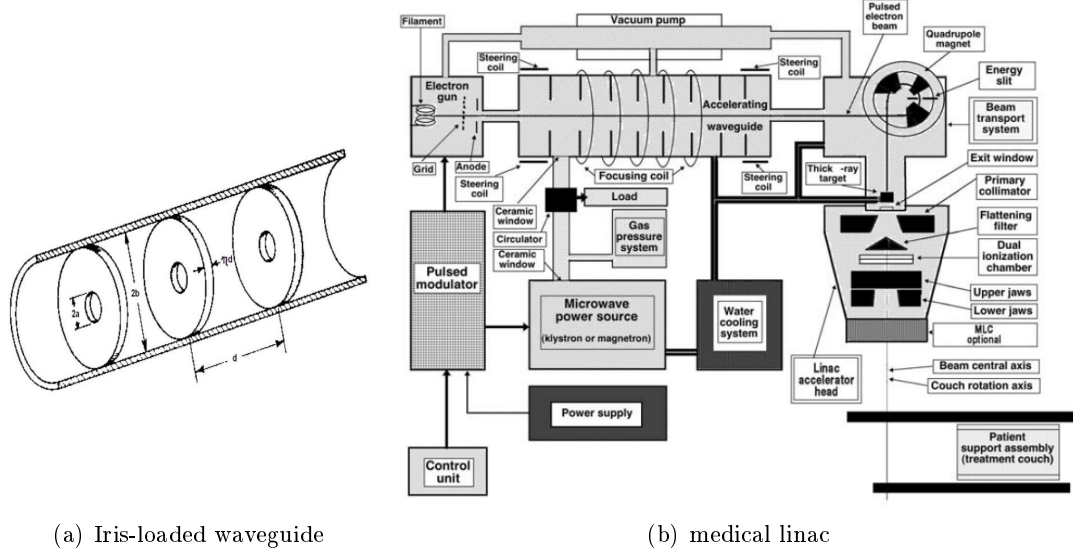(a) Iris-loaded waveguide   (b) medical linac

Figure 1.2: a) Iris-loaded waveguide of an electron-LINAC [23]. b) Components of a medical linear accelerator [52].

radio frequency (RF) power generator which consists of the RF power source and the pulsed modulator. The RF power source can be a klystron or magnetron which uses the acceleration and deceleration of electrons in vacuum for the production of high power RF fields [52].

For the transport of the accelerated electron beam to the bremsstrahlungs-target, evacuated drift tubes, steering and focusing coils, as well as bending magnets are used. Depending on the LINAC's arrangement, different electron bending systems can be used, such as $90°$, $112.5°$ or $270°$. Thereby, the electron beam is guided onto the bremsstrahlung-target, whereby photons (as described in section 1.1) are produced. The subsequent path of the generated photon beam in the treatment head will be described in section 1.4 [52]. Despite the bremsstrahlungs-target, the primary collimator, and the flattening filter, the treatment head consists of various components (figure 1.3 and 1.2(b)). Additionally, there are secondary collimators and jaws, which are adjustable blocks used to shape the field of the LINAC. For precise tumor irradiation and sparing of the surrounded healthy tissue, a multi-leaf-collimator (MLC) is used. The MLC consists of leaves of a high Z-material arranged in pairs which continuously move during treatment to shape the treatment beam. Thereby, treatment quality can be improved. Furthermore, lead, brass or steel wedges can be placed inside the treatment head. They enable the productin of a tilt dose profile which can further improve treatment quality [52].

For LINAC output monitoring, a transmission ionization chamber, which is independent of temperature and pressure, is placed between the flattening filter and the second collimators. This enables permanent monitoring of the beam output during patient treat-

ment. For additional safety, i.e. to prevent the failure of one chamber, the treatment head consists of a second, absolutely independent ionization chamber. The ionization chambers measure monitor units (MU) which are defined as follows [38, 52]:

> "The monitor chamber reads 1 MU when 1 cGy is delivered to a point at a given depth in the phantom with the surface of the phantom positioned so that the specified point is at the isocenter of the machine and the fields size is 10 cm x 10 cm at the isocenter." (Mayles P, Handbook of Radiotherapy Physics - Theory and Practice, 2007, p. 434)

1.4 Flattening Filter Free Photon Beams

With regard to photon beam therapy, two kinds of photon beams have to be distinguished. There are flattened photon beams, which are characterized by their flat dose profile and the resulting uniform dose distribution. Due to the fact that a photon beam, generated by the bremsstrahlungs-target of low-Z material, has a forward peaked dose profile, a flattening filter (FF) has to be used. The conically-shaped filter consists either of a medium- or high-Z material and is thicker in the center in order to produce the characteristic flat profile. As shown in figure 1.3(a), the flattening filter is positioned behind the primary collimator which defines the maximum circular field size through the conical shape and the absorbing material (e.g. tungsten) [22, 52].

(a) flattened photon beam   (b) unflattened photon beam
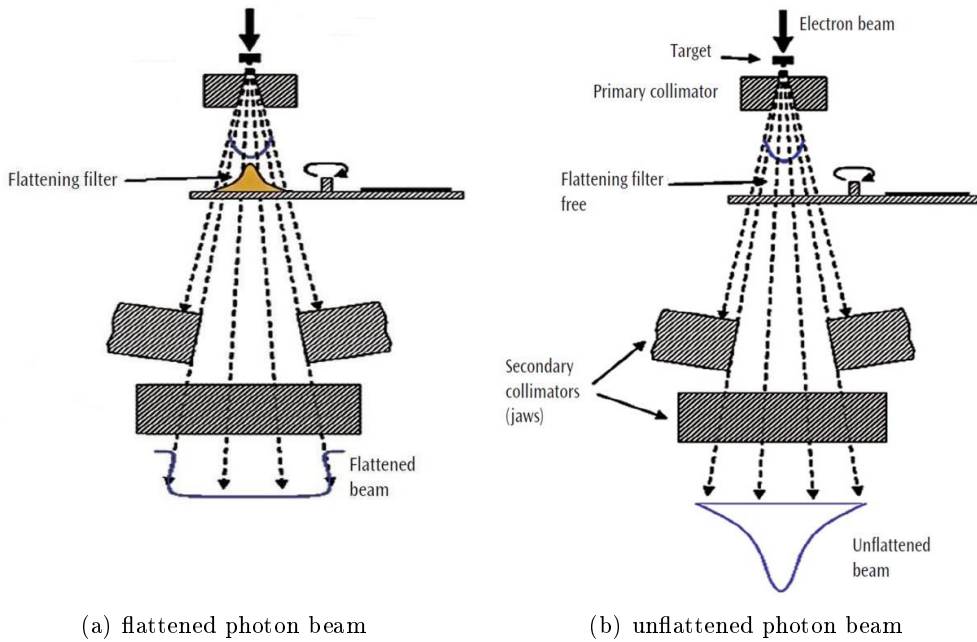
Figure 1.3: Components of a treatment head for a) flattened and b) unflattened photon beams. [15]

Unflattened photon beams have already been in use for several years now. They are characterized by a pronounced peak which gets more pronounced with higher energies. The main improvement of using flattening filter free (FFF) photon beams is the higher dose rate. Thereby, the treatment time can be significantly reduced, whereby the patient's comfort can be improved. Especially for lung treatment the reduced delivery time improves treatment accuracy due to the reduction of tumor displacement during respiration motion [22, 65].

Unflattened photon beams bring about additional improvements. The lack of the flattening filter reduces photon scattering, whereby the variation of the head-scatter factor with field size is reduced. Leakage of the treatment head can be reduced up to 65 % for 10 MV photon beams [33]. Additionally, photon attenuation in the FF leads to a reduction of energy with increasing distance from the central axis. This effect is called off-axis softening and can be reduced by using unflattened photon beams. The missing flattening filter in unflattened photon beams also results in a lower production of contamination electrons. This reduction decreases the variation of the depth of the dose maximum with field size. The reduction of theses effects leads to an improvement of calculation accuracy [22, 32].

The missing filter and the thereby softer beam result in a higher surface and skin dose, especially with regard to small field sizes and low energies. To avoid this, larger field sizes and higher energies should be used in combination with unflattened beams. Similarly, the whole body integral dose is higher for unflattened photon beams and low energies. This can again be avoided by using higher energies. [22].

The peripheral dose (PD) to surrounded tissue can be divided into three groups. First, the PD far from the field edge (about 20 cm) is caused by leakage and scatter in the treatment head. Due to the fact that the lack of the filter decreases leakage and scatter, the PD can be reduced by 23 % for 6 MV photon beams and up to 31 % for 10 MV photon beams [33]. Second, closer to the field edge, the soft energy spectrum leads to more patient scatter and, thereby, to a higher a PD. Third, the PD close to the field edge is again reduced for unflattened beams [22, 33].

1.5   Detectors

There are various types of detectors with partially different functions. Some detectors only detect the number of particles per time without detecting their energy. Other detectors allow tracking of the particle's path. Additionally, there are detectors to measure the energy of incoming particles, like semiconductor-, scintillation detectors or ionization chambers [14].

1.5.1   Ionization Chambers

In the context of this study, ionization chambers are used for the detection. They consist of two electrodes within a gas-filled chamber, between which a voltage is applied.
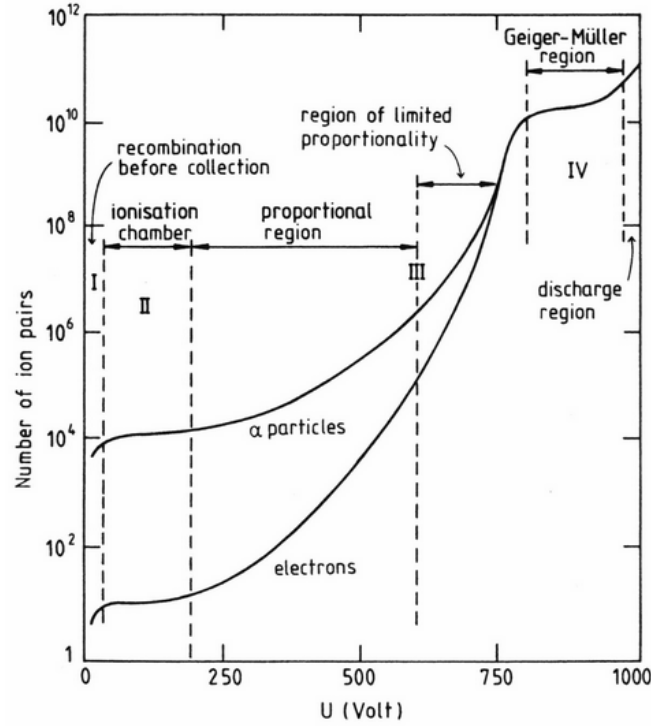
Figure 1.4: Different regions of operation for ionization chambers depending on the applied voltage [35].

An incoming particle interacts with the gas atoms whereby ions and free electrons are produced. Due to the applied electric field, these charged particles move to the electrodes. Thereby, a measurable current is created. As shown in figure 1.4, the applied voltage leads to different operation modes. If the applied voltage is too low, the ionized particles interact with gas particles of opposite charge, and thus, recombine to neutral atoms before they can be detected (region I). The second region is the operation region for ionization chambers. In this so-called saturation region all ions and electrons can be detected. Further increase of the applied voltage leads to the production of secondary particles due to additional ionization of the gas. This region is called proportional region because the detected signal is proportional to the incoming particles. The second part of region III leads to an increase in the creation of secondary particles whereby the proportionality is limited. In the fourth region, the voltage is so high that each incoming particle causes an avalanche of secondary particles so that the detected signal is not proportional to the incoming particle anymore. This operation mode is called Geiger-Müller region. In this region, each particle produces the same signal, independent of the energy. Finally, a further increase leads to independent gas discharge [14, 38].

1.5.2   Radiochromic Films

In comparison to ionization chambers, which allow to measure point doses only, radiochromic film enable the measurement of a two-dimensional dose distribution.

Radiochromic films consist of polyester layers enclosing one ore more layers of monomer. The monomer layer is radiosensitive and due to the impact of ionization radiation a polymerization reaction is induced. This polymerization results in a coloration of the monomer layer proportional to the absorbed energy. The polymerization reaction stabilizes after a film-specific time; thereafter the films can be scanned.

Advantages of these films are the tissue equivalent material and the insensitivity to visible light (but not UV light), compared to radiographic films. Radiographic films contain silver bromide crystals which induce a chemical reaction when light or ionization radiation interact with the crystals. The disadvantage of these films is the need of a photochemical process to wash off all not affected crystals to get the darkened image. Similar to radiochromic films the amount of silver left on the film after the photochemical process is proportional to the radiation, however, radiochromic films are sensitive to light which furthermore complicate the usage [9, 55].

1.6   Computed Tomography

Due to the excellent soft tissue contrast computed tomography (CT) is a good and common choice for the definition and localization of tumors [52].

In a simplified way it can be explained that during a CT scan a X-ray beam rotates around the patient (similar to the gantry during radiation therapy) and special X-ray detectors detect the transmitted beam. Depending on the tissue the X-ray beam is differently attenuated due to different stopping powers of the tissues (e.g. bone or lung-tissue). Based on the measured attenuation coefficient a linear transformation to Hounsfield units (HU) can be made. The various Hounsfield units belong to special tissue, as for example a HU of -1000 belongs to air, -500 belong to lung tissue, 0 belongs to water and a HU between 700 and 3000 belongs to bone. This enables an improved determination of the tissue out of CT density data.

As a result of the CT rotation, 3D volumetric information of the patient can be gained [42, 52].

During the localization of lung tumors room laser can be used for accurate patient positioning and marking and additionally, respiration belts are used which enable to link images with breathing signals. Thereby, 3D-CT scans can be connected to a special breathing phase which enable the generation of 4D-CT scans including the breathing phases. This allows the simulation of tumor motion due to respiration.

1.6.1   Cone Beam Computed Tomography

For imaging using a cone beam computed tomography (CBCT) an X-ray source and an X-ray detector are fixed to the gantry. While the gantry rotates around the patient a divergent pyramidal- or cone-shaped X-ray beam is radiated through the area of interest

and detected by the opposite located flat panel X-ray detector. In comparison to the previously explained CT, only one rotation around the patient is used for a CBCT due to the fact that images of the entire field of view are taken [56].

As a result of one scan for the entire field of view the image quality is limited. Thereby, the main use of CBCT scans are positioning checks and tumor tracking during radiation therapy.

1.7   Volumes and Margins for Treatment Planning

In preparation for radiation therapy, different volumes are defined and delineated on the CT scans. These volumes are an important resource for treatment planning.

1.7.1   Gross Tumor Volume

"The gross tumor volume (GTV) is the gross palpable or visible/demonstrable extent and location of malignant growth." (ICRU Report 50, p. 6)

The GTV delineates the primary tumor and the possible metastases. Due to the fact that the GTV defines the volume with the largest tumor cell density it should receive the highest dose [27, 28].

1.7.2   Clinical Target Volume

"The clinical target volume (CTV) is a tissue volume that contains a demonstrable GTV and/or subclinical microscopic malignant disease, which has to be eliminated. This volume thus has to be treated adequately in order to achieve the aim of therapy, cure or palliation." (ICRU Report 50, p. 6)

This volume includes small cell clusters or any malignant cells which cannot be detected or seen on the CT scan [27, 28]. For patients whose tumor has been removed during surgery, there is no GTV. As such, only the CTV will be delineated for post-operative irradiation [29].

1.7.3   Internal Target Volume

The individual scans with the delineated CTVs are superposed and an internal target volume (ITV), which encloses all CTVs, is generated. Additionally, an internal margin, which compensates for variations in size, shape, position of the tumor and physiologic movements, can be added but is not done in the clinic [27]. For cases where uncertainties in the CTV location plays an important role, the ITV is a helpful task to generate a proper volume for irradiation [29].

1.7.4 Planning Target Volume

To ensure that the whole ITV receives the prescribed dose, CTV movement due to patients' irregular respiration or stirring has to be considered. Additionally, uncertainties in positioning and variations in the beam geometry have to be considered. Therefore, the ITV has to be geometrically enlarged, whereby the planning target volume (PTV), which is the main volume for treatment planning, is created [27, 28].

1.7.5 Respiration Management

The first methods for the consideration of tumor motion due to respiration are so-called motion-encompassing methods. For one of these methods a slow CT scans can be taken which means that CT scans are averaged so that multiple respiration phases are recorded per slice. Another motion-encompassing method is the inhale and exhale breath hold CT. For this method two different CT scans are taken. However, it assumes that the patient is able to hold the breath. The last of these methods is the 4D respiration-correlated CT scan and is the method used for the patients within this study. The process of this method was described in section 1.6.
However, these methods do not consider that the respiration motion can change between imaging and treatment [3].
The next methods are respiratory gating methods. An example of these methods is the attachment of reflective markers on the patient's body. The motion of the attached markers is than analyzed by a software which controls the linear accelerator [24].
Furthermore, breath-hold methods can be used for respiratory management. One example of these methods is deep-inspiration breath-hold which reduces tumor motion and additionally changes internal anatomy to improve OAR sparing. Active-breathing control is another method for respiration management for which a spirometer connected to a balloon valve is used for breath control.
Two other breath-hold methods are the self-held breath-hold method with or without respiratory monitoring. Using this technique the patient has to hold the breath at some point in the breathing cycle during which the dose is delivered.
A different respiration managing method is called forced shallow breathing. During this method a frame including a plate is pressed against the abdomen of the patient so that the chest motion and, thereby the tumor motion, can be reduced while the patient can breath more or less freely [3].
Real-time tumor tracking is another method for managing the respiration motion wherefore various methods are available nowadays.
The use of any of these methods enables the reduction of the applied margins and, thereby, reduces the volume to be irradiated, which, in turn allows better organ at risk sparing.

1.8 Treatment Methods

For the planning of different treatment methods two different treatment planning techniques, forward and inverse treatment planning, have be distinguished. Using forward treatment planning, the beam geometry, such as the number of beams, beam angles, shape, wedges or collimators are defined manually before the calculation of the dose distribution can be started. The settings are controlled manually until the best possible distribution is achieved. In contrast to that, inverse treatment planning operates with defined constraints for the PTV and OARs. The treatment planning system then calculates the dose distribution depending on the chosen constraints. After the first calculation the constraints can be further adjusted to receive the best possible treatment plan [61].

1.8.1 3D Conformal Radiation Therapy

Three-dimensional conformal radiation therapy (3D-CRT) uses static beams for treatment planning. Since it is calculated using forward treatment planning, the beam parameters, such as the number of beams, beam direction, beam weights, collimator shapes and wedges have to be chosen manually before the dose distribution can be calculated [48].

1.8.2 Dynamic Conformal Arc Therapy

Dynamic conformal arc therapy (DCAT) enables an irradiation while the treatment head rotates around the patient. During the rotation the beam is set towards the center of the tumor while an MLC defines the shape which has to be irradiated. While the treatment head moves around the patient, the leaves of the MLC are moving to define the area which has to be irradiated and, thereby, protect the surrounding organs from being irradiated. In contrast to volumetric modulated arc therapy the beam is not modulated which reduces dosimetric errors induced by small field. Instead, the field shape is adapted to the projection of the tumor. [62].

1.8.3 Volumetric Modulated Arc Therapy

Volumetric modulated arc therapy (VMAT) is a treatment method which combines intensity modulation and beam rotation. VMAT is similar to intensity modulated arc therapy (IMRT enables the modulation of the intensity during treatment) but combines the modulation with the irradiation of any arc length (up to $360°$) around the tumor instead of separated, static beams. This causes a reduction of treatment time from approximately 20 minutes using IMRT to around 2 minutes using VMAT. Thereby, uncertainties caused by organ displacement can be reduced which leads to higher treatment accuracy and an increase in the patient's comfort.
Similar to the other treatment plans VMAT uses a MLC to adapt the leaf's position during irradiation, as well. Furthermore, it is possible to change the dose rate, the field

configuration, the rotation velocity of the treatment head, and the angle of the MLC to improve the dose distribution of the planning target volume [43].

1.9   Monte Carlo Simulation

The Monte Carlo (MC) simulation is an accurate method for dose calculation in radiation therapy. It is a stochastic method for solving complex equations (in this case transport equation) numerically by the use of random numbers [8, 19].

Especially for heterogeneous tissue, MC simulation provides more accurate results than other calculation methods, such as, for example, the pencil beam method which provides high quality results in homogeneous tissue (e.g. brain) but overestimates doses in heterogeneous regions [8]. Since the lung tissue is covered by various tissues, such as bones (particularly ribs) and air, Monte Carlo simulation is the best choice for the simulation of the dose distribution for lung tumor treatment.

Monte Carlo simulation combines the simulation of the particles in the treatment head and the simulation of the particles in the patients. The simulation of the particles path within the treatment head depends on the bremsstrahlungs-target, the collimators, the flattening filter, as well as particle absorbance and deviation by the MLC. Furthermore, electron contamination has to be taken into account. To avoid a full MC simulation of the particle's path in the treatment head, a so-called mutli-source-model can be used. This model consists of two Gaussian-shaped photon sources which are placed near the bremsstrahlungs-target and the flattening filter, and a uniform electron source. Using the virtual energy fluence model, the dose can be calculated on the following condition: the amount of contaminating electrons P_e and photons P_γ is equal to 1, and the amount of photons P_γ is composed of the primary P_0 and scattered photons P_S.

$$
\begin{aligned}
P_e + P_\gamma &= 1 \\
P_\gamma = P_0 + P_S &= 1
\end{aligned}
\tag{1.16}
$$

These equations are the base for the Monte Carlo calculation of the dose distribution using the virtual energy fluence model [19]. Using this first simulation, the energy, position, and angle of the impinging particle can be calculated.

As a next step the paths of the particles (histories) within the patient are calculated. Therefore, the histories of the particles are simulated until the entire energy of the particle is absorbed or the particle and the secondary particles have left the volume of interest [19]. Each interaction between the particles and molecules of the tissue changes the momentum and energy of the particles, and can additionally cause secondary particles. These interactions are simulated by using a total cross section, which describes the interaction probability of a particle, and a differential cross section, which describes the probability of generating secondary particles. For the numerical calculation of the transport equation defined by the cross sections, random numbers are used.

The accuracy of the simulation can be improved by increasing the number of particle histories. However, the more particle histories are used for the simulation, the longer the time of calculation [8, 19].

1.10   Purpose and Aim

The main ambition of this study was to compare treatment plans for patients with lung tumors using flattened and unflattened photon beams. Therefore, VMAT and DCAT plans using flattened and unflattened photon beams were generated for 10 different patients using the Monaco treatment planning system. For the generation of the treatment plans two dose prescriptions were used. The first dose prescription follows the clinical protocol for stereotactic body radiation therapy (SBRT) and is already used for lung cancer treatment. The second dose prescription is the recommended by the ICRU report 83 and leads to steeper dose-volume-histogram at higher doses. This recommendation allows to cover the target with higher doses and thereby potentially reduces the interplay-effect.
Generating different Monaco plans allowed for the evaluation of flattened and unflattened photon beams and the comparison of different treatment methods.
All generated plans were compared to clinically used 3D-CRT plans which were in turn generated with the Oncentra Master Plan (OMP) system by Elekta (Stockholm, Sweden). Therefore, the OMP plans were imported to the Monaco system to enable precise comparison.

For the evaluation of the treatment methods the dose distribution for the PTV and OARs, and the dosimetric effect of target motion were considered. This so-called interplay effect, which depends on the tumor's motion and the treatment method, has an influence on the dose coverage of the target. Due to respiratory motion, the tumor can move out of the irradiation field, whereby the dose to the target can be reduced [63]. To investigate this, the treatment plans for four patients were irradiated onto a breathing phantom which enabled the simulation of respiration motion. For 2-dimensional detection of the dose distribution a film was placed inside the phantom. To evaluate the interplay effect, the plans were irradiated onto the phantom without motion and two different motion types.

Moreover, the dose calculation accuracy of the Monaco treatment planning system was evaluated by comparing the calculated dose distribution with the measured dose distribution using the static mode of the phantom.

2 | Materials and Methods

2.1 Patient Cohort

For this study ten recently treated patients with lung metastases, in either the left or the right lung (one with metastases in both sides), were randomly selected. The patients were treated using unflattened 3D conformal radiation therapy which was planned with Oncetra Master Plan (Elekta, Stockholm, Sweden).
To evaluate different treatment methods volumetric modulated arc therapy and dynamic conformal arc therapy plans were generated for flattened and unflattened photon beams using the Monaco 5.00.04 system. All plans were generated using the SBRT and ICRU dose prescription which will be explained in detail in section 2.3.3. While treatment plans were generated for ten different patients, the measurements, described in section 2.7, were done only for four different patients due to the fact that the phantom could only be used for patients with the tumor in the left lung. Additionally, a complete set of treatment plans (3D-CRT, VMAT and DCAT) were generated based on the anatomy of the phantom.

2.2 Treatment Preparation

In preparation for the radiation therapy 4D-CT scans were acquired of each patient. For treating lung tumors CT scans of five different breathing phases were created using a breathing belt. The breathing phases were 0%, 50%, and 100% in inspiration as well as 0% and 50% in expiration. On each of the 5 CT scans a CTV was delineated. Afterwards the CT scans with the delineated CTVs were superposed, and an ITV, which included all CTVs and thereby all possible tumor positions during respiration motion, were delineated. To prevent the tumor from moving out of the irradiation field, an additional $4\,\text{mm}$ margin was added to the ITV. The ITV in combination with the margin provided the PTV which was the main volume for treatment planning.

2.3 Treatment Planning

All treatment plans within this study were generated using the treatment planning system (TPS) Monaco 5.00.04 from Elekta (Stockholm, Sweden). It uses a Monte Carlo

algorithm for dose calculation and thereby allows an accurate and fast dose calculation [40]. To improve the accuracy of the photon and electron distribution a virtual source model using two Gaussian shaped photon sources, which are located close to the bremsstrahlungs-target and to the flattening filter, and an electron source are used [19]. The size of the calculation grid was chosen to a grid spacing of 3 mm and the statistical uncertainties of the Monte Carlo simulation were chosen to 1 % uncertainty per control point.

2.3.1   Equivalent Uniform Dose

The Monaco software enables the use of cost functions which consider the biological response of normal tissue to dose and the biological volume effect. Using a biological function, the treatment planning software looks at voxel-regions, instead of single voxels, due to the fact that a higher dose can be tolerated if less volume is irradiated. The biological functions use the concept of equivalent uniform dose (EUD) for the calculation of the biological effect caused by a homogeneous dose which is, in turn, based on the known inhomogeneous dose [53].

Tissue irradiated with a homogeneous dose D and tissue irradiated with an inhomogeneous EUD, which is equal to the dose D, exhibit the same tissue damage. This is the case because the dose D and the EUD cause the same biological effect [44, 68, 25]. The equivalent uniform dose can be calculated for normal tissue as well as tumor tissue by using the tissue specific parameter a:

$$EUD = \left[\frac{1}{N} \sum_i D_i^a \right]^{\frac{1}{a}} \tag{2.1}$$

In this equation N is the number of voxels and D_i is the dose in the ith voxel [68].

Other important parameters concerning dose evaluation of organ at risk (OAR) are the biological effective dose (BED) and the equivalent uniform dose in 2 Gy fractions (EQD$_2$). Since some organs are more sensitive to irradiation than others, the BED defines which effect a specific dose will have on the specific organ at risk. The biological effect E of a single radiation dose d can be described by a linear quadratic equation E=(αd + βd^2) which contains the organ specific parameters α and β [38]. This implies that the BED, which is delivered in specified fractions n, depending on the dose d and the tissue specific ratios α/β, can be calculated as follows [37]:

$$BED = nd \left[1 + \frac{d}{\alpha/\beta} \right] \tag{2.2}$$

A more common and practical parameter for clinical use is the biological equivalent dose. It describes the dose which is equivalent to an irradiation with 2 Gy fractions. It can be calculated with the use of the BED (equation 2.3) or the use of the total dose D, and the dose per fraction d, which is shown in equation 2.4 [37]:

$$EQD_2 = \frac{BED}{1 + \frac{2}{\alpha/\beta}} \tag{2.3}$$

$$EQD_2 = D \left[\frac{d + \alpha/\beta}{2 + \alpha/\beta} \right] \tag{2.4}$$

Both equations include the tissue specific parameter α/β which enables the calculation of the EQD_2 depending on the individual OAR.

2.3.2 Cost Functions

The Monaco treatment planning system generates treatment plans depending on various cost functions and their chosen parameters. An example for a treatment plan generated with Monaco is shown in figure 2.7.
All used cost functions and parameters which were used for the plans, generated within this thesis are shown in appendix A. The position of the cost function in the list of the *IMRT Constraints* (figure 2.2) determines the assignment of the voxels. This means that if some structures overlap, the position of the cost function determines which voxels belong to which structure. Figure 2.1(a) shows a voxel assignment wherefore the cost function for the PTV was positioned before the function of the rectum and vice versa in figure 2.1(b).
The plus signs in the column of *Relative Impact* state how difficult it is to accomplish the prescribed isoconstraint. The more plus signs (up to four), the more difficult it is [57, 36, 17].
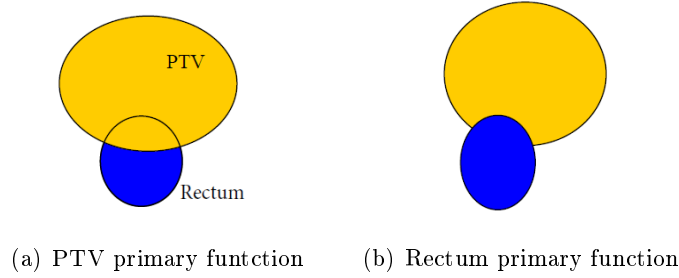

(a) PTV primary funtction   (b) Rectum primary function

Figure 2.1: Layering depending on the position of the cost functions [17].

Structure	Cost Function	Enabled	Status	Manual	Weight	Reference Dose (Gy)	Multicriterial	Isoconstraint	Isoeffect	Relative Impact
PTV	Target EUD	✓	On	☐	1.00			40.500	44.673	
	Quadratic Overdose	✓	On	☐	0.01	65.000		0.020	0.000	
Lung right	Parallel	✓	On	☐	0.12	13.400	☐	1.00	1.01	++++
Lung left	Parallel	✓	On	☐	0.01	13.400	☐	8.50	7.90	
Heart	Serial	✓	On	☐	0.04		☐	5.000	4.993	++
Stomach	Serial	✓	On	☐	0.02		☐	5.000	5.016	++
Myelon	Serial	✓	On	☐	0.01		☐	3.000	2.988	
Oesophagus	Serial	✓	On	☐	0.01		☐	4.500	4.509	+
Body	Quadratic Overdose	✓	On	☐	0.02	30.000	☐	0.400	0.382	+
	Quadratic Overdose	✓	On	☐	0.01	39.800	☐	0.100	0.048	
	Quadratic Overdose	✓	On	☐	0.23	20.000	☐	1.150	1.165	++++
	<click to add a new structure>									

Figure 2.2: Example of cost funtions for a VMAT plan.

Target EUD

The target equivalent uniform dose (EUD) cost function is one of two main cost functions for PTVs. This cost function is a biological one and can be adapted by choosing the cell sensitivity value which fits the target structure.

For this function a prescribed dose for the target, between 100 cGy and 15000 cGy, and, as already mentioned, a *Cell Sensitivity* value (between 0.10 and 1.00), has to be chosen. A high cell sensitivity value leads to more target volume being irradiated with the prescribed dose and vice versa. This may lead to some confusion because a high cell sensitivity means that the cells are more sensitive to irradiation.

Additionally, optional physical parameters can be activated. The first one, *Surface Margin*, can be helpful if the target is near the patient's surface because it reduces problems with the dosimetric build-up effect. The second parameter, *Optimize over all voxels in volume*, extends the cost function to the total volume of the structure. This can be useful if there is another structure overlapping the PTV [57, 36, 17].

Target Penalty

The other main cost function is a physical function and is called *target penalty* cost function. It allows entering the minimum volume which has to be irradiated, whereby the probability to reach the PTV coverage increases.

Required parameters for this function are the prescribed dose (*Prescription*) [Gy] and the *Minimum Volume* [%]. Similar to the Target EUD function, a prescribed dose for the target, between 0 cGy and 20000 cGy, has to be chosen. In the context of this cost function, the prescribed dose acts as a minimum dose which has to be reached. The parameter for *Minimum Volume* (0 to 100 %) determines the volume which has to receive the prescribed dose [57, 36, 17].

The physical parameters for this function are the same as mentioned in chapter 2.3.2
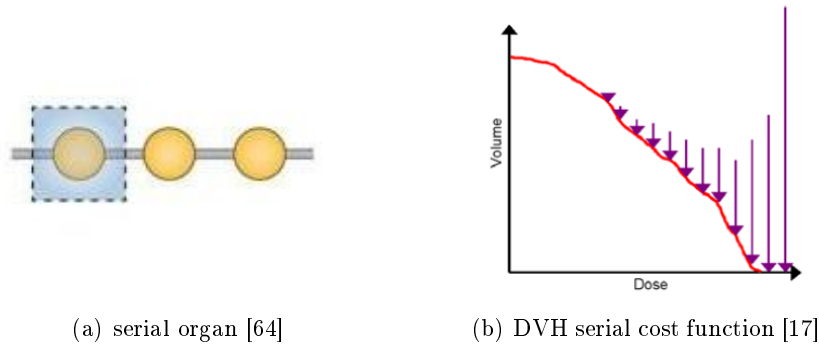

(a) serial organ [64]   (b) DVH serial cost function [17]

Figure 2.3: serial cost function

Serial Cost Function

The serial cost function should be used for serial organs at risk, for instance, the heart, myelon or oesophagus. For these organs even a small irradiated volume can lead to the failure of the entire organ (figure 2.3(a)). Therefore, the serial cost function reduces even small volumes of hot spots within the serial organ.

The serial cost function depends on an *Equivalent Uniform Dose*, which is the variable isoconstraint for this function and ranges from 100 cGy to 15000 cGy. Another required parameter is the *Power Law Exponent* (k value), which defines the shape of the dose-volume-histogram (DVH) for the organs at risk. This k value ranges from 1 to 20 and should be adapted to the serial organ. A small k value results in a smooth curve, which means that there is a slight decrease of the dose. A large k value, however, results in a considerable decrease of dose at a certain point. As shown in figure 2.3(b), the serial cost function reduces the dose at the tail of the DVH curve, to reduce hot spots in the OARs.

Additionally, there are optional physical parameters like *Shrink Margin*, *Optimize over all voxels in volume*, and *Multicriterial Optimisation*. By using Multicriterial Optimization, the Monaco system reduces the dose for the chosen organ as far as possible without reducing the PTV coverage. The physical parameter called *Shrink Margin* enables to choose a distance [cm] within the voxels are ignored during optimization [57, 36, 17].
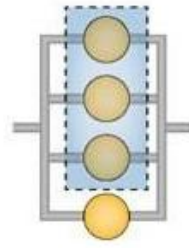
Parallel Cost Function

The parallel cost function is the main function for parallel organs, such as the lung, liver or kidney, i.e. organs which can be damaged by a certain volume without failing entirely (figure 2.4(a)).

The required parameter for this function is a *Reference Dose* (100 cGy to 10000 cGy), which is the equivalent uniform dose that can be irradiated to the organ without damage. Since parallel organs can tolerate some partial irradiation damage, the isoconstraint for this function is the *Mean Organ Damage* [%]. Similar to the serial cost function, a *Power Law Exponent* (range from 1 to 4) is necessary for this parallel cost function. In contrast to the serial cost function, a small k value in the parallel cost function means that volumes with high and low doses are equally weighted, whereas a large k value leads to a higher weighting of volumes with a higher dose. Figure 2.4(b) shows that the parallel cost function reduces the dose in the middle of the DVH curve in order to reduce the volume which is irradiated [57, 36, 17].

Additionally, there are the same *Optional Physical Parameters* to choose as mentioned for the serial cost function.

Quadratic Overdose Cost Function

The quadratic overdose cost function enables the limitation of hot spots in the PTV and OARs. This cost function can be used in combination with one of the previous functions to limit the maximum dose for the PTV or OAR. This function can also be
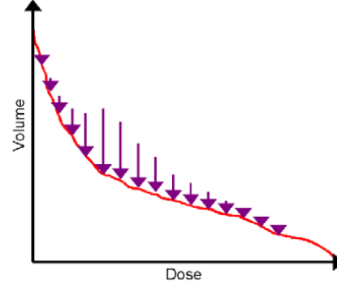
(a) parallel organ [64]   (b) DVH parallel cost function [17]

Figure 2.4: parallel cost function

used without another cost function to reduce the dose which is exposed to the entire body. Therefore, more quadratic overdose functions with different maximum doses can be used for one organ.

This function requires a *Maximum Dose* (between 0 Gy and 150 Gy) which works as a threshold dose. Additionally, a value between 2 and 1500 cGy for the RMS (root mean square), which defines the acceptable dose range, has to be chosen [57, 36].

For this function there is the opportunity to choose the same optional physical parameters as for the previous sections.

Overdose DVH

The overdose DVH cost function limits the volume which receives a specific dose below a chosen limit. Therefore, the *Objective Dose* [Gy] and the *Maximum Volume* [%] are the required parameters. As shown in figure 2.5(a), this cost function controls the DVH at one point [17]. Within this study this function is used to limit the near-minimum dose of the ICRU plans.
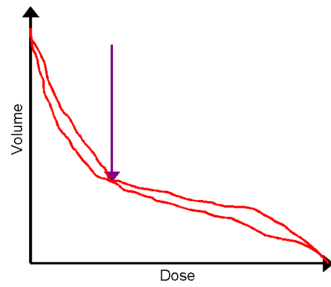
(a) Influecne of the Overdose DVH function on the dose-volume-histogram[17].
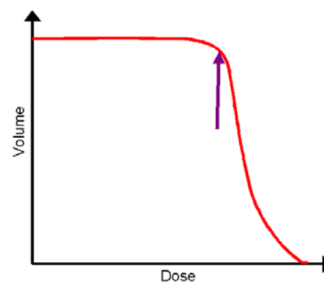
(b) Influecne of the Underdose DVH function on the dose-volume-histogram[17].

Figure 2.5: DVH curves influcenced by two different functions.

Underdose DVH

The underdose DVH cost function defines the volume which receives at least a specific dose. An *Objective Dose* [Gy] and the percentage of the *Minimum Volume* [%] which receives the dose have to be chosen [17]. As shown in figure 2.5(b), this cost function induces a steeper dose fall-off.

Additional Adjustments

In the context of this study there are two additional sequencing parameters which have to be considered.
One of these parameters is *Segmentation Shape Optimization*. Using this parameter, the Monaco TPS refines the segment shapes and thereby improves plan quality. This sequencing parameter is used for all VMAT and DCAT plans throughout this study.
The other parameter, called *Target Margin*, was used mostly for the DCAT plans and some ICRU plans. It changes the margin around the target and thereby the Monaco system includes more or less voxels (depending on the chosen parameter) around the target during optimization. To improve the plans the target margin *very tight* was chosen, which means that a margin between 0 mm to 1 mm is used during optimization [57, 36, 17]. Using this property PTV coverage of DCAT and sometimes VMAT plans were improved.

Beams

Using the Monaco TPS it is possible to switch between different treatment methods at the beam dialog box (*Delivery* in figure 2.6(a)). Furthermore, it is possible to choose between photon beams of 6 MV and 10 MV (10 MV beams are used within this thesis) and between flattening filter and flattening filter free photon beams.
Further properties can be adapted in the beam dialog boxes, for example, the *Isocenter Location*. Different locations of the isocenter of the beam can be chosen. In this study, the isocenter was set to *Center of PTV* .
For each patient the arcs have to be adjusted individually to prevent the irradiation of organs at risk and thereby reduce the dose. The irradiation through the healthy side of the lung (side without tumor or metastases) should be avoided. Additionally, an angle range which is reduced to the necessary range reduces treatment time and thereby reduces the chance of tumor displacement.
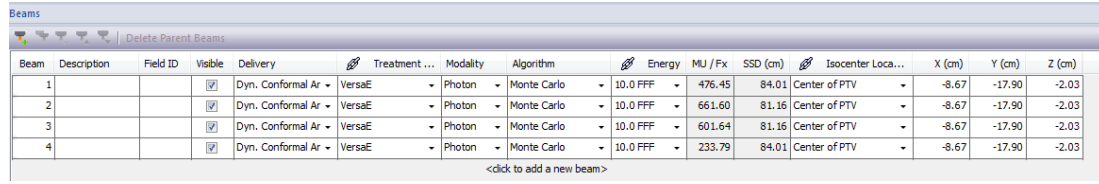Due to the arrangement of the hardware (e.g. wires) the gantry cannot irradiate a full arc and has to be stopped at 180°. Thereby, for some patients, an irradiation range consisting of two arcs has to be used (e.g. 45-180 and 180-250°). An example of this is shown in figure 2.6(b).
It is also possible to choose the irradiation direction clockwise and counterclockwise (shown in figure 2.6(b) at the *Dir* column), enabling irradiation of one arc twice. This increases the degrees of freedom, whereby an improvement of the treatment plan can be achieved. For DCAT plans the irradiation direction was chosen clockwise and counterclockwise. Thus, the maximum dose for the PTV increased and additionally achieved

a PTV coverage of 99% without increasing the lung dose considerably.

For other plans it was possible to irradiate only a small range of the arc twice so that the PTV conformity can be increased. However, each additional irradiation range increases treatment time and, thereby, may reduces accuracy.
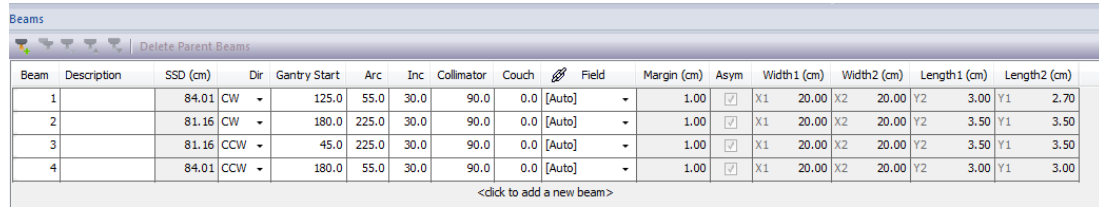
Using the Monaco TPS it is possible to choose between different collimator angles. Therfore, this thesis considered different collimator angles of $0\,°$, $5\,°$, and $10\,°$ and ultimately proved that for VMAT plans a collimator angle of $90\,°$ provides the best coverage and conformity. The best collimator angle for the DCAT plans, however, varies between $5\,°$ or $90\,°$.

(a) Beam General Properties: Enable the choice of the treatment method, the modality, the energy, the algorithm for calculation, and the location of the isocenter.

(b) Beam Geometry: Selectable parameters are the number of beams, the starting point of the gantry and the arc, the irradiation direction, and the adjustment of the collimator.

Figure 2.6: Screenshot of the beam adjustments in the Monaco software. Depicted are the general beam properties (a) and the beam geometry (b).

2.3.3   Dose Prescription

The prescribed dose for the plans used in this study was $D_P = 62.3$ Gy in 3 fractions (20.8 Gy per fraction).

All plans were designed using two different dose prescriptions. The first one was the clinically used stereotactic body radiation therapy (SBRT) prescription which prescribes 65 % of the dose to 99 % of the PTV. This leads to a dose of 13.5 Gy per fraction and a total dose of 40.5 Gy. The reason for the use of this dose prescription is, on the one hand, due to clinical experience and on the other hand, the possibility of the reduction of the interplay effect caused by the use of more, in detail three, fractions.

In addition, another dose prescription using multiple dose-volume constraints was used for the treatment plans. ICRU Report 83 [29] states that the use of multiple constraints leads to more precision in treatment planning. This report stipulates that the near-

minimum dose $D_{98\%}$ should reach at least 95 % of the prescribed dose. Similar to that, the near-maximum dose $D_{2\%}$ is defined to be less than ideally 107 %, but at least less than 110 % of the prescribed dose. The median dose $D_{50\%}$ is defined as $D_P \pm 2$ Gy. Due to these constraints, the dose-curve in the dose-volume histogram of the ICRU plans is shifted to higher doses and exhibit a steeper dose fall-off than the SBRT plans. This enables the compensation of a drop of dose due to the interplay effect and is the main reason for the use within this thesis.

In the context of the ICRU prescription, clinical prescription stipulates that at least a volume of 95 % should receive a dose of at least 95 % of the prescribed dose, which equals a dose of 59,2 Gy. This reduction of the irradiation volume is done because it is not possible for all patients to irradiate 98 % of the PTV with 95 % of the prescribed dose due to limitation of the planning system and treatment machine.
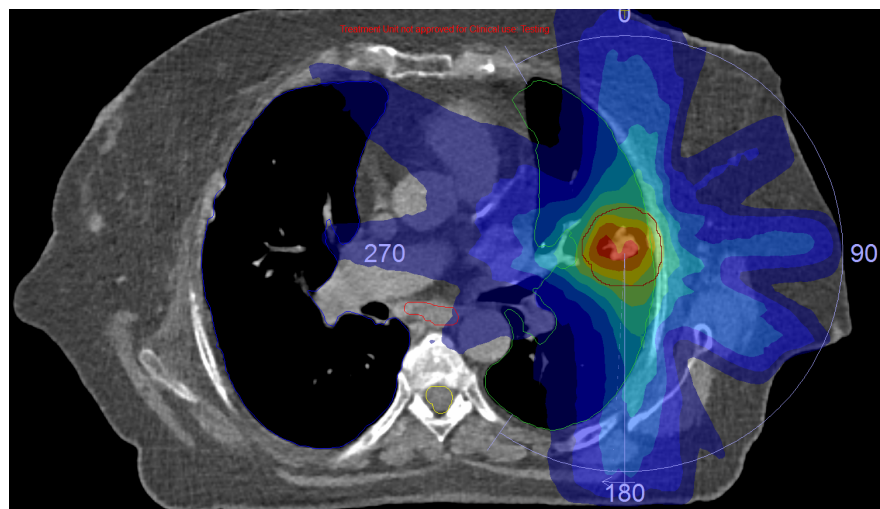
(a) transverse plane
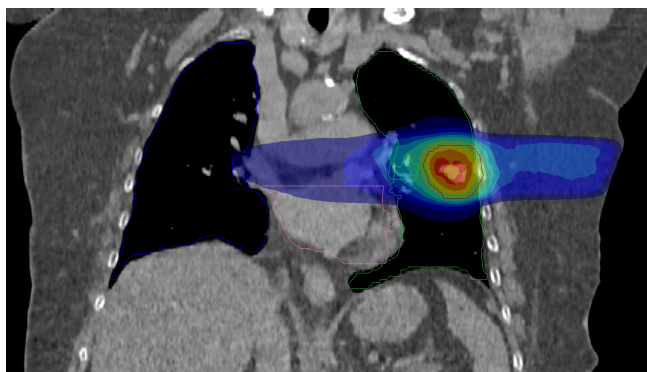
(b) coronal plane
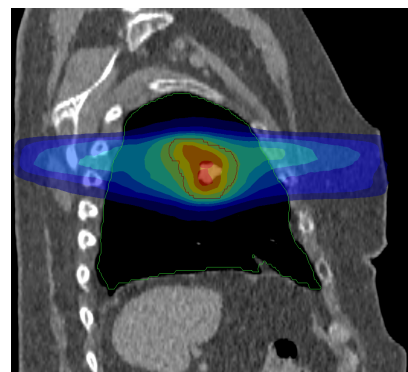
(c) sagittal plane

Figure 2.7: Dose distribution of Monaco planned unflattened SBRT VMAT plans in a) transverse b) coronal and c) sagittal view.

2.3.4   Evaluation of Treatment Plans

For the evaluation of the treatment plans limits for the doses used for organs at risk were defined. The maximum dose ($D_{0.1cc}$) for the myelon was limited to 5 Gy per fraction whereas the maximum doses for the esophagus and the stomach were limited to 6 Gy per fraction. No strict limit was defined for the heart, but the dose per fraction should be as low as possible.

For the ipsilateral lung an EQD_2 of 20 Gy, which equals a physical dose of 13.4 Gy, was limited to an irradiation of maximal 20 % of the lung volume. Compared to the ipsilateral lung, the contralateral lung should receive a smaller dose. Hence, the EQD_2, which is limited to 20 % of the volume of the contralateral lung, is reduced to 5 Gy (physical dose of 5.3 Gy).

To evaluate the dose to the tumor tissue, the near-minimum, near-maximum and median dose of the PTV were compared. In addition, the median dose of the ITV was considered because it should get the highest dose.

In order to compare the plan quality of the treatment methods in detail, the conformity index (CI) of the treatment plans was calculated. The conformity index results from the quotient of the volume of the target covered by the prescribed isodose (TV_{PIV}) squared and the volume of the target (TV) multiplied with the volume of the prescribed isodose (PIV) [50]:

$$CI = \frac{TV_{PIV}^2}{TV \cdot PIV} \qquad (2.5)$$

For a perfect match of the dose to the target, the conformity index would have the value 1, which means that 100% of the target volume is irradiated. Whereas a conformity index of 0.60 specifies that 60% of the target is irradiated. The lower the CI, the less conformity the plan has. Using this index the overtreatment is evaluated as bad as the undertreatment [50].

Due to the fact that different dose prescriptions are used for the treatment plans, the CI is calculated for different isodoses: as such, $CI_{95\%} = 59.2$ Gy, $CI_{80\%} = 49.84$ Gy, $CI_{65\%} = 40.5$ Gy, $CI_{50\%} = 31.2$ Gy and $CI_{40\%} = 24.9$ Gy. This enables the comparison of the plan quality of all treatment plans despite their different dose prescriptions.

To highlight the differences of the treatment methods, the average and standard deviation of DVH-curves for the individual plans were calculated and plotted using a MATLAB script. Thereby, treatment methods were compared using their DVH-curves.

2.4   Breathing Phantom

For the measurements an in-house developed breathing phantom called ARDOS (Advanced Radiation Dosimetry System) was used. This phantom enables the simulation of the patient's respiration motion during radiation therapy.

The phantom consists of different components of tissue-equivalent materials. As depicted in figure 2.8(a) the outer part of the phantom is a conical torso consisting of tissue-equivalent solid water with a density of $1.05 \, \text{g/cm}^3$. The conical shape simulates

the motion of the chest during respiration. The "ribs", which are made of bone equivalent tissue $(1.4 \, \mathrm{g/cm^3})$, are positioned underneath this cylindrical torso. The inner cylinder, which represents the lung, is made of lung-equivalent high density balsa wood $(0.3 \, \mathrm{g/cm^3})$ and tissue-equivalent solid water [30, 31]. A tomographic picture, which illustrates the different materials, is shown in figure 2.8(b).

(a) Components of the phantom.   (b) Tomogram
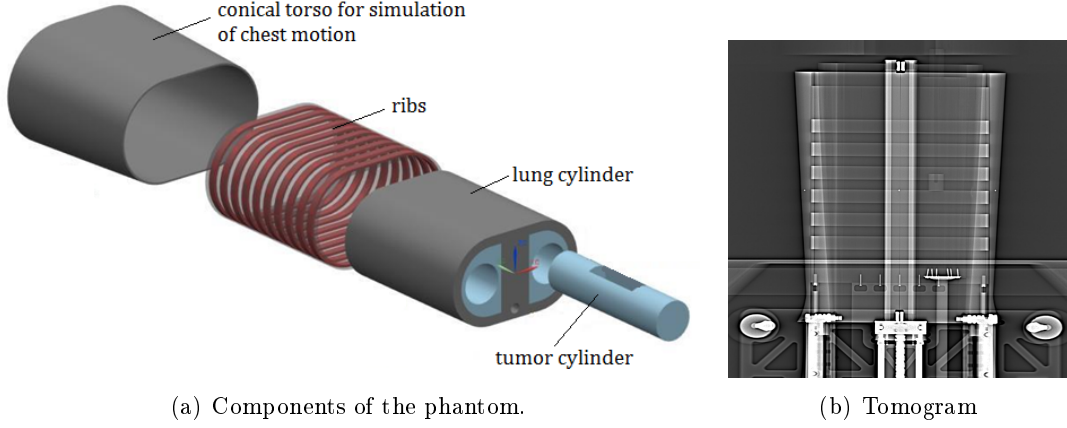
Figure 2.8: Setup of the ARDOS breathing phantom: a) shows the different components of the phantom and b) shows a tomographic picture of the phantom which illustrates the different materials, such as ribs. [30, 31]

For the detection of the radiation, cylindrical tubes are cut out of each sides of the balsa wood. Inside this cylinder, detectors are placed in another cylinder. Various detectors, such as thermoluminescence dosimeters, pinpoint ionization chambers and films can be used. Due to their spatial resolution, films were used in this study. The cylinder consists of high density balsa wood and a 2.5 x 2.5 $\mathrm{cm^2}$ cylindrical volume of tissue-equivalent solid water to represent the tumor. Within this solid water the films were placed as shown in figure 2.10(b).

To simulate 3D tumor motion, the phantom enables four different motions on the left side of the lung. The tumor can move up to 10 cm in longitudinal direction (movement in y-direction in figure 2.9(b)) and can also rotate up to 360°, whereby movement in x- and z-direction can be simulated (figure 2.9(a)).

To simulate the chest motion during respiration the phantom provides rib motion up to 10 cm in y-direction, while the outer cylindrical torso provides movement up to 4 cm to simulate chest motion.

A combination of the different movements (chest motion, rib motion, longitudinal and rotational tumor motion) can be simulated using a basic sine wave. Additionally, the frequency of the motion, which illustrates the breathing rate, can be chosen. Each type of motion starts from its initial position and moves in one direction [30, 31].

The phantom is operated using an Arduino script where the motion steps of the four different movements, the breathing rate and the sine wave can be inserted.

(a) Phantom x and z-direction.

(b) Phantom y-direction.
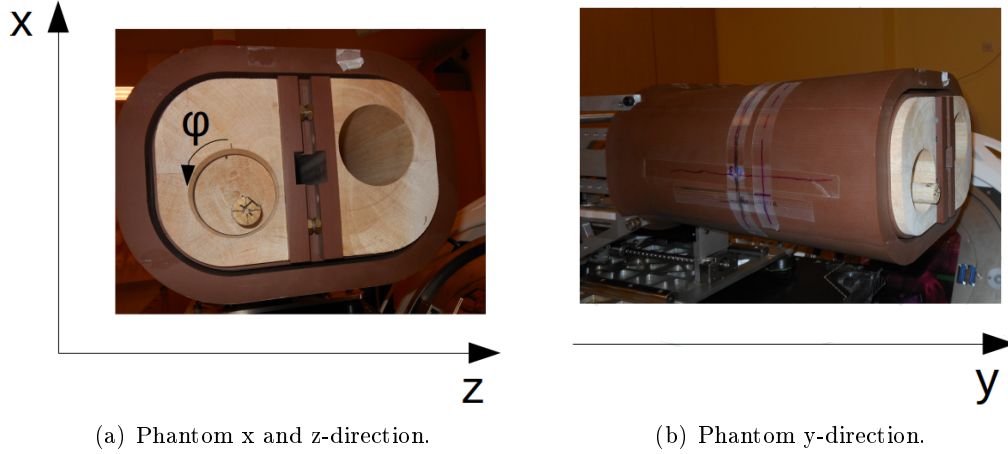
Figure 2.9: Illustration of the breathing phantom.

2.5   Radiochromic Films

Radiochromic films were used within this study because they provide a high spatial resolution in combination with little energy dependence and near tissue-equivalence [16]. For this work GAFChromic EBT3 films (Ashland ISP, Wayne, NJ) of the lot number #04141402 with the expiration date of April, 2016 were used. All films were cut to a size of 2.5 x 2.5 cm^2 to fit into the tumor of the phantom. To ensure that all films were scanned and positioned in the phantom the same way, the films were marked in the lower right hand corner.

The EBT3 films which were used within this work do not need any chemicals for development. Additionally, they do not require a dark room because the are room-light safe. The optimal dose range for EBT3 films is between 0.2 and 10 Gy, whereat the dynamic dose range reaches up to 20 Gy.

The film consists of two layers of 125 μm matte-polyester enclosing 28 μm (can vary between different lots) of an active layer, consisting of the active component, a marker dye and other components (e.g. stabilizers). [5].

All films were scanned before and after irradiation using an Epson Perfection V700 Photo scanner which enables reflective scanning. On the one hand, the films were scanned before irradiation to get a background value, and to get the structure of the film (potential scratches due to the preparation or inhomogeneities due to the film production) on the other hand. To ensure that all films were scanned at the same position in the scanner, a mask, which positions the film in the middle of the scanner, was used. After the warm-up of the scanner all films were scanned twice in portrait orientation to make sure that all films are scanned under the same conditions. The films were scanned with 48-bit color and a spatial resolution of 150 dpi without any scanner correction.

The irradiated films were scanned around 48 hours after the irradiation due to possible post-irradiation coloration under the same conditions as the non-irradiated films.

The scanned data was saved as tagged image file format (tiff) image files and loaded to ImageJ (U. S. National Institutes of Health, Bethesda, Maryland, USA) to choose a region of interest (ROI) of a size of 140 x 140 pixel. Using ImageJ each ROI was split into a red, green and blue channel.

The chopped data was loaded into a MATLAB script which calculates the net optical density of all films using the following equation:

$$netOD^i(D_j) = log_{10} \left(\frac{I_{unexp}^i(D_j) - I_{bckg}}{I_{exp}^i(D_j) - I_{bckg}} \right) \tag{2.6}$$

where I_{unexp}^i and I_{exp}^i are the gray values for unexposed and exposed i^{th} films and I_{bckg} is the value of the blank scan, which is equal to 2^{16} [16].

For the conversion of the netOD to dose values a calibration curve for dose values ranging from 1 to 35 Gy in dose steps of 2 Gy was done. For this the films were cut into a size of 4 x 4 cm^2 and irradiated separately for flattened and unflattened photon beams with a field size of 10 x 10 cm^2 and a focus-to-skin distance of 90 cm. Furthermore, each film was placed between 10 cm of solid water above and 15 cm of solid water under the film. Using the net optical density and the known dose values, a fitting curve using a exponential function (equation 2.7) for flattened and unflattened photon beams, each for the green and red channel, was calculated.

$$f(x) = a \cdot e^{b \cdot x} + c \cdot e^{d \cdot x} \tag{2.7}$$

2.6 Linear Accelerator

All measurements were done using the Elekta Versa HD linear accelerator. This LINAC enables an irradiation with 6 MV and 10 MV flattened and unflattened photon beams. The size of the treatment field can be up to 40 x 40 cm^2. To shape the photon beam the LINAC features an MLC consisting of 160 leaves with a width of 5 mm. Compared to other MLCs, which enable a leaf movement of 20 $\frac{mm}{s}$, the leaves of this MLC are able to move with a speed of 35 $\frac{mm}{s}$. The leaves are positioned on a dynamic leaf guide which can further improve the speed of the leaf motion up to 65 $\frac{mm}{s}$ [10, 18].

The calibration of the LINAC was done in such a way that for a source-to-surface dose of 90 cm, a penetration depth of 10 cm and a field size of 10 x 10 cm^2 a dose of 1 Gy corresponds to 100 MU.

2.7 Irradiation Process

For four patients with the tumor on the left side of the lung and for the phantom itself the nine different plans were radiated to the breathing phantom. As already mentioned, films were used for the detection. Figure 2.10(b) shows the cylinder including the tumor in which the film was placed.

For each patient all plans were irradiated during three different phantom motions. First

the plans were irradiated to the static phantom without motion. Furthermore, a longitudinal motion of 1 cm and a herein denoted realistic motion, which was a combination of translateral and rotational tumor motion, was used during irradiation. The realistic motion was patient specific and reproduced the tumor motion during the 5 CT scans which were done before treatment planning. To reproduce the tumor motion the x, y and z-coordinates of the center of CTVs of the 5 breathing phases were compared to the center of the PTV. Thereby, the movement of the tumor in all three directions, based on the center of the PTV, which was the isocenter of all plans, was calculated.

Knowing the movement in all directions and the dimensions of the cylinder (figure 2.10(a)) the angle of the rotational motion of the tumor can be calculated using basic trigonometry.
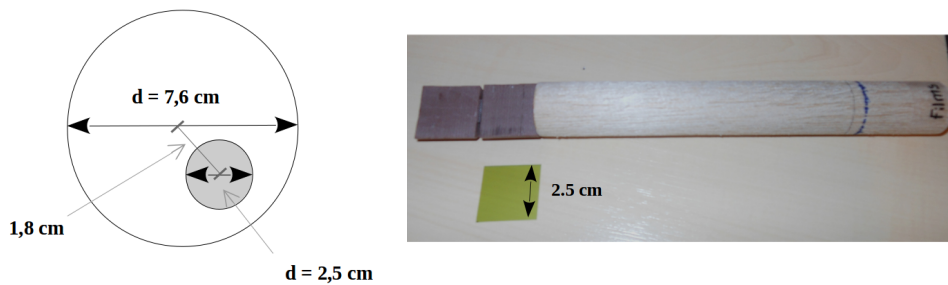
(a) Dimensions of the lung and tumor cylinder for the calculation of the tumor rotation.

(b) Lung cylinder including the tumor for the film positioning.

Figure 2.10: Dimensions of lung cylinder and tumor cylinder.

As already mentioned in section 2.4, the phantom moves in one direction starting at the isocenter. Due to the motion of the patient's tumor in positive and negative y-direction, the isocenter was shifted for some patients to enable the movement in both directions. Due to the conical shape of the phantom, this may led to a variation of the thickness of the material and thereby to a different dose to the target.

As mentioned above, the phantom's tumor was positioned in the isocenter of the LINAC. For this a marker was placed on the phantom indicating the center of the tumor. Nevertheless, a CBCT scan, which checked the positioning, was done at the beginning of each measurement day. To additionally reduce uncertainties caused by inaccurate positioning or daily fluctuations, all measurements of one patient, including static, translateral and realistic motion, were done on the same day.

The evaluation of the dose distribution of the different phantom movements during irradiation (static, longitudinal and realistic motion) was done by comparing minimal, maximal, and median dose values derived from film measurement. Due to film defects at the edges of the film (caused by cutting) the minimum doses were calculated using the 0.025-quantile. For the evaluation of the dose distribution across the entire film, 2-dimensional plots and line profiles of the different movements were extracted.

To check the output of the LINAC, verification measurements were done on each mea-

surement day. Doing that, a farmer ionization chamber (Farmer PTW 30006) was placed between 10 cm of solid water plates above and 15 cm of solid water plates below the farmer ionization chamber (figure 2.11(b)). Due to the fact that an RW3 solid water plate had to be used for the positioning of the ionization chamber, a correction factor had to be considered. A cross calibration of solid water and liquid water identified that a correction of 1 % was necessary. This procedure is based on Seuntjens et al. 2005 "Absorbed dose to water reference dosimetry using solid phantoms in the context of absorbed-dose protocols". Thus, 1 cm of the 10 cm solid water plates above the phantom had to consist of the plate for the ionization chamber, 1 mm of RW3 solid water and 2 mm of the standard solid water plates. Using this setup the ionization chamber was placed at the center of a 10 x 10 cm^2 field at a focus-to-skin distance of 90 cm. The chamber had to be connected to an electrometer (PTW Unidos 1) which had to be adjusted to the ionization chamber *#11 "Waterproof 0.6"*, to the modus $\int$ *Strom dt*, to the measurement range *Med 11 nA*, and to a voltage of 400 V. For this output check 200 MU were irradiated using 6 MV and 10 MV flattened and unflattened photon beams. For the calculation of the dose some values, such as the cobalt calibration value of the ionization chamber, a conversion factor for cobalt to dose, a correction factor for temperature and pressure, a correction value for polarity, and a saturation correction factor are needed. The polarity correction factor depends on the polarity of the chamber's voltage which, in turn, depends on the construction of the chamber. The saturation correction factor is caused by the recombination of charge carriers which decrease the signal. According to the Bragg-Gray cavity theory the measured Coulomb value is related to the absorbed dose. Using the previous mentioned factors, partially obtained from the LINAC calibration, the dose values [Gy] can be calculated following the IAEA technical report series (TRS) 398.

For the evaluation of the planning accuracy of the software, the measured dose distribution of the films were compared to the planned dose distribution. To be able to do this, a quality assurance (QA) plan was recalculated to the phantoms structure. Thus, the planned dose distribution of the plans, for those patients which were used for the measurements, were recalculated to the phantom structure. Afterwards a matlab script, which compared the dose matrices on the basis of the maximum dose values of rows and columns, respectively was used. Thereby, the dose profiles for the calculated and measured doses were best possible matched. This enabled the comparison of the measured and calculated dose distribution by the evaluation of minimal, maximal, and median dose values. Additionally, 2-dimensional plots of the dose distributions of the measured and calculated doses enabled the evaluation of the dosimetric accuracy.

(a) Breathing phantom positioned in home position.

(b) Setup of RMI solid water and RW3 solid water plates for the verification of the LINAC output using a farmer ionization chamber.
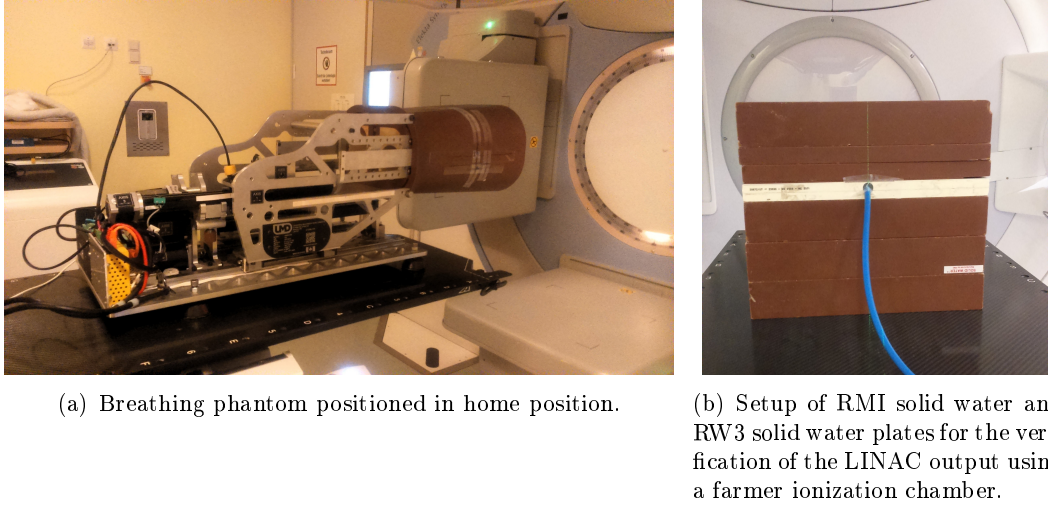
Figure 2.11: Setup of the breathing phantom and setup for the verification of the LINAC output.

2.8 Statistical Analysis

The statistical analysis of the calculated dose values, as well as the measured dose values, were executed using Tukey's honestly significant difference (HSD) test. Therefore a MATLAB script, which pairwise compares the honestly significant difference between two means, was generated.

Using the HSD test, the critical value $q_{\alpha,A}$ for A groups and an α level of 0.05 (for a significant difference) and 0,01 (highly significant difference) were taken from a table of the "Critical Values of the Studentized Range Distribution" [34]. This table lists the critical values depending on the number of the groups A and the degrees of freedom (dfe), which was calculated by subtracting the number of groups from the absolute number of values N. The absolute number of values was defined as the size of the groups S multiplied with the number of the groups A. Thereby the HSD value can be calculated as:

$$HSD = q_{\alpha,A}\sqrt{\frac{MS_s(A)}{S}} \tag{2.8}$$

whereat $MS_s(A)$ is the mean value of the variance of each group.

In the final step the mean values of each group were subtracted from each other. If the absolute value was greater than the HSD value, the difference was not significant, whereas if the absolute value of the subtraction was less than the calculated HSD value, it stated a significant difference [1].

Following this method, a matrix, which compares the mean values of each group, was obtained.

3 | Results

3.1 Dose Distribution

In an initial step the calculated dose distribution of the different treatment plans were evaluated. Therefore, the generated Monaco plans were compared to the clinically used 3D-CRT treatment plans.
Table 3.1 summarizes characteristic parameters of all treatment plans. For the target volume the patient averaged physical dose were used, whereas for the OARs the mean biological dose values were evaluated. The significance of the differences were calculated using Tukey's honestly significant difference test (described in section 2.8).

Target Coverage

The comparison of 3D-CRT plans with the other SBRT treatment plans showed that no significant differences concerning PTV coverage, or dose distribution for PTV and ITV occurred. Only the flattened SBRT DCAT plans showed a very significant decrease of the near maximum dose of around 5 % and 7 % for unflattened and flattened plans, respectively. Additionally, the unflattened SBRT DCAT plans showed a significant reduction of the mean and near min dose. In comparison, the plans calculated using the dose prescription of the ICRU report 83 exhibited a very significant increase of the dose to the PTV and ITV, such as, for example, the increase of the mean dose from 51.4 Gy for 3D-CRT to 63.7 Gy for ICRU VMAT FFF plans. However, the PTV coverage of the ICRU plans were significantly reduced and only significant different for the DCAT plans.
Due to the different dose descriptions, the CI of 95 % of the prescribed dose was significantly increased for the ICRU plans. Compared to the 3D-CRT plans, the other conformity indices ($CI_{80\%}$, $CI_{65\%}$, $CI_{50\%}$ and $CI_{40\%}$) were highly significantly decreased for all ICRU plans. This decrease of the CI describes a lower conformity for the ICRU plans. As an example for the reduction of the conformity for the ICRU plans, figure 3.1 illustrates the dose near the isocenter. The red circle delineates the PTV, while the different colors illustrate different dose ranges as shown in the scale. As an example, the green area defines the dose range of 65 % of the prescribed dose (equals 40.5 Gy). For the SBRT plans perfect conformity would be stated with $CI_{65\%} = 1$; then the green area would match with the red line of the PTV.

Table 3.1: Evaluation of treatment plans compared to the clinically used unflattened 3D-CRT plans: the significant * (p-value < 0.05) and highly significant ** differences (p-value < 0.01) were calculated using Tukey's HSD test.

	SBRT ($D_P = 40.5\,$Gy)					ICRU ($D_P = 59.2\,$Gy)			
	FFF			FF		FFF		FF	
	3D-CRT	VMAT	DCAT	VMAT	DCAT	VMAT	DCAT	VMAT	DCAT
PTV coverage [%]	98.6±0.5	99.1±0.1	99.2±0.2	99.1±0.2	99.1±0.2	98.3±0.3	95.7±0.6**	98.2±0.2	95.7±0.7**
PTV(D98%) [Gy]	41.0±0.6	41.7±0.4	41.8±0.7	41.9±0.7	42.7±3.2*	59.5±0.3**	58.3±0.4**	59.2±0.4**	58.2±0.5**
PTV(D50%) [Gy]	51.4±1.7	51.7±1.5	49.7±2.0	52.2±2.6	49.1±2.1*	63.7±0.5**	63.8±1.2**	63.7±0.4**	62.8±1.3**
PTV(D2%) [Gy]	61.3±1.3	62.9±1.1	58.0±3.1**	62.7±1.1	57.0±2.8**	66.9±1.6**	69.6±2.27**	66.8±1.3**	68.6±2.1**
ITV(D50%) [Gy]	55.5±2.6	57.4±1.4	52.8±4.1	57.0±1.8	52.7±1.9	63.9±0.5**	66.2±1.2**	64.0±0.6**	65.4±0.9**
Lung IPS V_{20EQD2} [%]	9.3±5.4	8.7±4.5	11.2±5.3	8.7±4.5	10.9±5.1	14.5±6.7	22.1±10.8**	14.3±6.4	20.4±9.2*
Lung CON V_{5EQD2} [%]	2.2±3.3	1.2±0.9	0.1±0.2	1.3±1.1	0.2±0.1	2.2±1.8	1.5±2.2	2.4±2.0	1.3±3.0
Myelon $D_{0.1ccEQD2}$ [Gy]	9.0±5.1	3.2±1.8	10.1±5.8	3.4±1.4	9.5±5.0	5.7±3.6	16.2±14.0	5.6±3.5	15.0±11.6
Esophagus $D_{0.1ccEQD2}$ [Gy]	10.4±6.4	4.8±1.6	9.4±5.5	4.7±2.1*	8.7±3.5	8.3±2.5	11.3±4.1	7.8±3.1	11.1±4.4
Heart [1] $D_{0.1ccEQD2}$ [Gy]	0.2±0.1	0.2±0.2	0.2±0.1	0.3±0.2	0.2±0.2	0.4±0.3	0.6±0.4	0.5±0.3	0.6±0.4
Heart near tumor $D_{0.1ccEQD2}$ [Gy]	30.4±3.0	20.0±3.6	23.4±8.8	18.5±2.2	24.0±9.6	54.7±19.9	46.6±25.3	55.0±21.0	39.4±15.6
Stomach [2] $D_{0.1ccEQD2}$ [Gy]	20.4	16.2	35.1	18.5	40.0	27.4	72.4	29.7	46.3
$CI_{95\%}$	0.10±0.05	0.14±0.05	0.06±0.04	0.14±0.08	0.03±0.03	0.69±0.07**	0.67±0.07**	0.71±0.09**	0.69±0.08**
$CI_{80\%}$	0.57±0.11	0.60±0.09	0.42±0.14*	0.60±0.11	0.38±0.17**	0.40±0.07**	0.30±0.04**	0.41±0.07*	0.32±0.06**
$CI_{65\%}$	0.68±0.04	0.73±0.06	0.61±0.13	0.74±0.06	0.64±0.12	0.24±0.05**	0.17±0.03**	0.24±0.05**	0.19±0.04**
$CI_{50\%}$	0.38±0.05	0.37±0.05	0.30±0.07	0.39±0.03	0.30±0.07	0.13±0.03**	0.10±0.02**	0.13±0.03**	0.15±0.13**
$CI_{40\%}$	0.23±0.03	0.21±0.03	0.19±0.05*	0.21±0.03	0.18±0.04**	0.08±0.02**	0.07±0.01**	0.08±0.02**	0.07±0.02**
MU/fx	2354±152	4183±699**	2299±195	4225±895**	2336±291	7981±1966**	2863±782	6933±1458**	2711±277

[1] For four patients the heart was close to the tumor. Hence, the evaluation was divided into "Heart" for those patients with the tumor far from the heart and "Heart near tumor" for the four patients with the heart close to the tumor.

[2] Only for one patient the stomach was in the region of irradiation.

The conformity indices for 80 % and 40 % of the prescribed dose were very significantly reduced for the flattened SBRT DCAT plans and significantly reduced for the unflattened SBRT DCAT plans. This is illustrated in figures 3.1(f) and 3.1(g).

Due to the improved conformity and the higher maximum dose for SBRT VMAT plans in comparison to SBRT DCAT plans, the conformity index $CI_{80\%}$ was highly significantly different and the $CI_{65\%}$ was also significantly different for these plans.

The SBRT plans showed the highest conformity index for $CI_{65\%}$ and the indices for higher and lower doses were reduced. In contrast, the ICRU plans showed best conformity for $CI_{95\%}$ and the indices for lower doses were reduced.

Figure 3.2 shows DVH which illustrate the average of the DVH curves for all patients. In figure 3.2(a) the dose-volume-histograms of the unflattened SBRT VMAT and SBRT 3D-CRT are illustrated. The figure shows that for the unflattened SBRT VMAT plans the PTV received a higher dose in addition to the improved dose conformity, which is shown in figure 3.1(c) and 3.1(d).

Similarly, the averaged dose-volume-histograms of flattened and unflattened SBRT VMAT plans are shown in figure 3.2(b). It illustrates that there were no differences concerning the doses to the PTV. The dose-volume-histograms in figure 3.2(c) compare the dose to the PTV for unflattened SBRT VMAT and DCAT plans. They depict that the near minimum doses were similar whereas the near maximum doses (D2%) showed a highly significant difference, with a dose difference of around 5 Gy (for flattened and unflattened SBRT plans).

The different dose prescriptions resulted in significant differences between SBRT and ICRU treatment plans. Figure 3.2(d) shows the averaged dose-volume-histograms of unflattened SBRT VMAT and ICRU VMAT plans. It shows significantly different dose-curves for the two plans and a higher dose with a steeper dose-fall-off for the ICRU VMAT plan. This differences in the dose-curve can be seen in all SBRT and ICRU plans.

Organs at Risk

The comparison of the dose to the ipsilateral lung showed that the volume which received an EQD2 of 20 Gy was significantly increased for ICRU DCAT (22.1 % for unflattened and 20.4 % for flattened) plans compared to 3D-CRT plans (9.3 %), whereas the other plans showed no significant difference concerning ipsilateral lung dose. These plans were not clinically acceptable due to the fact that they exceeded the clinical volume limit of 20 %. Comparably, the volume of the contralateral lung receiving an EQD2 dose of 5 Gy showed no significant differences.

Looking at the myelon, there were no significant differences in comparison to the clinically used plans. However, for one patient the flattened and unflattened ICRU DCAT plans exhibited too much dose to the myelon so that the dose was far above the prescribed dose limit (EQD2 D0.1cc = 57.2 Gy for flattened and 47.9 Gy for unflattened). The dose to the esophagus was acceptable for all plans and, especially for the SBRT VMAT plans, it was possible to reduce the averaged dose to 4.8 ± 1.6 Gy for flattened and 4.7 ± 2.1 Gy for unflattened plans.

In order to be able to compare the dose to the heart, it had to be determined whether the tumor was close to the heart or not. As is shown in table 3.1, there were very significant differences between the doses depending on the tumor location respective to the heart. The comparison with the clinically used plans showed no significant differences for both locations; however, the doses were increased for all ICRU plans.

The honestly significant difference test showed that no significant differences concerning OARs occurred for flattened and unflattened treatment plans. Furthermore, no significant differences for VMAT and DCAT plans were observed.

Despite the very large dose difference in the PTV for SBRT and ICRU VMAT plans, no significant differences concerning the dose to the lung and organs at risk were found. However, the average dose to the ipsilateral lung and partially the dose to the myelon were above the limit, but the differences were not significant. Similar to SBRT plans, no significant differences between the doses to the organs at risk occurred between ICRU DCAT and VMAT plans.

Monitor Units

The comparison of all plans with the clinically used plans showed very significant differences concerning monitor units per fraction (table 3.1). All VMAT plans (SBRT and ICRU) exhibited a very significant increase of the required monitor units. The monitor units for the SBRT VMAT plans were nearly twice as much as the monitor units for the clinically used plans, whereas the ICRU VMAT plans used monitor units which were almost four times higher than the used monitor units for the clinical plans.

The monitor units for SBRT VMAT plans almost doubled compared to SBRT DCAT plans; for ICRU plans the monitor almost tripled for VMAT plans compared to DCAT plans. Furthermore, the comparison of SBRT and ICRU VMAT plans exhibited a very significant difference concerning monitor units, whereas no significant difference occurred for DCAT plans.

(a) Transverse (or axial) view of the lung.

(c) 3D-CRT FFF

(d) SBRT VMAT FFF

(e) SBRT VMAT FF

(f) SBRT DCAT FFF

(g) SBRT DCAT FF

(h) ICRU VMAT FFF

(i) ICRU VMAT FF

(j) ICRU DCAT FFF

(k) ICRU DCAT FF
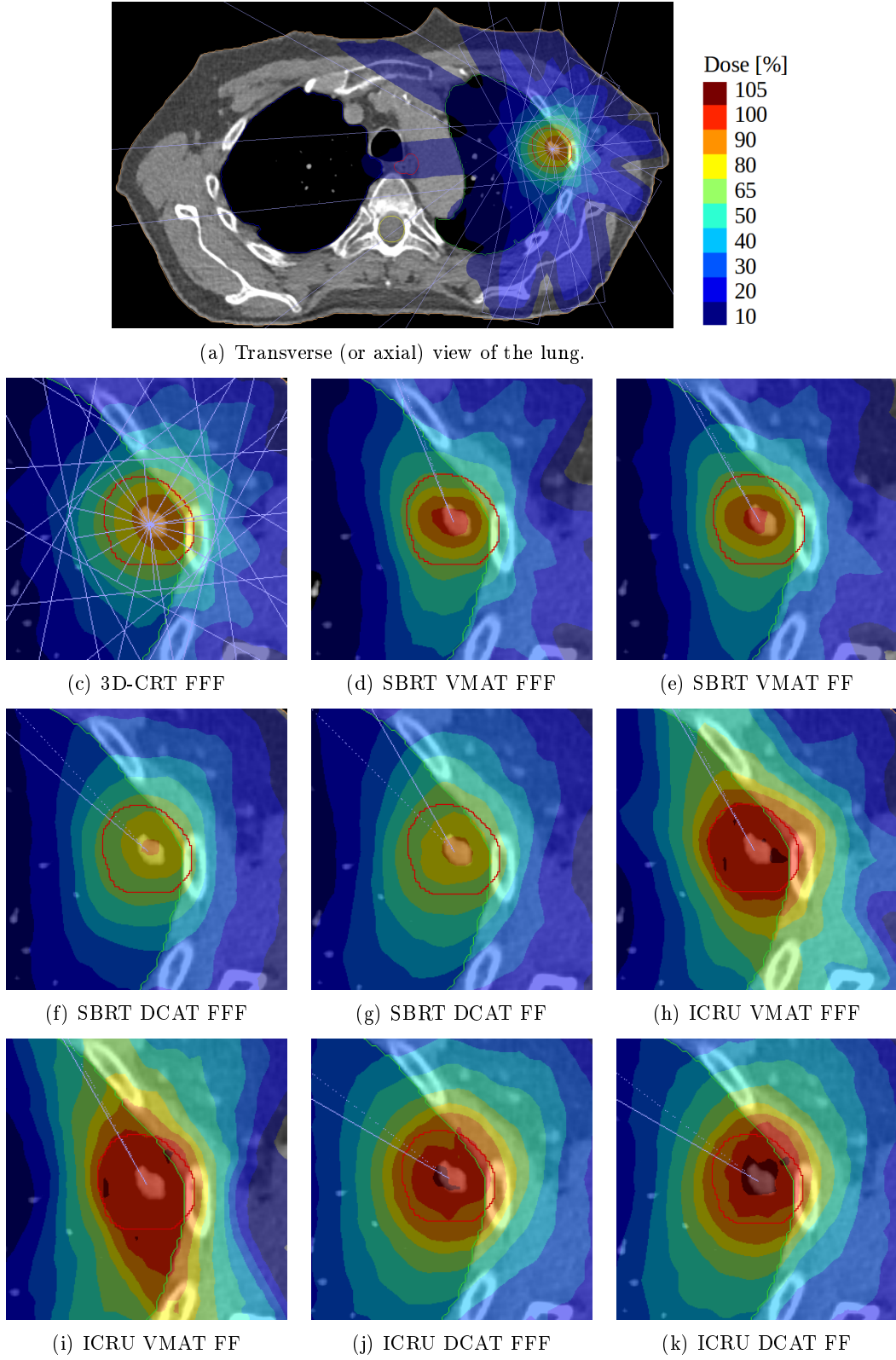
Figure 3.1: Comparison of the dose distribution of the PTV for all treatment methods.
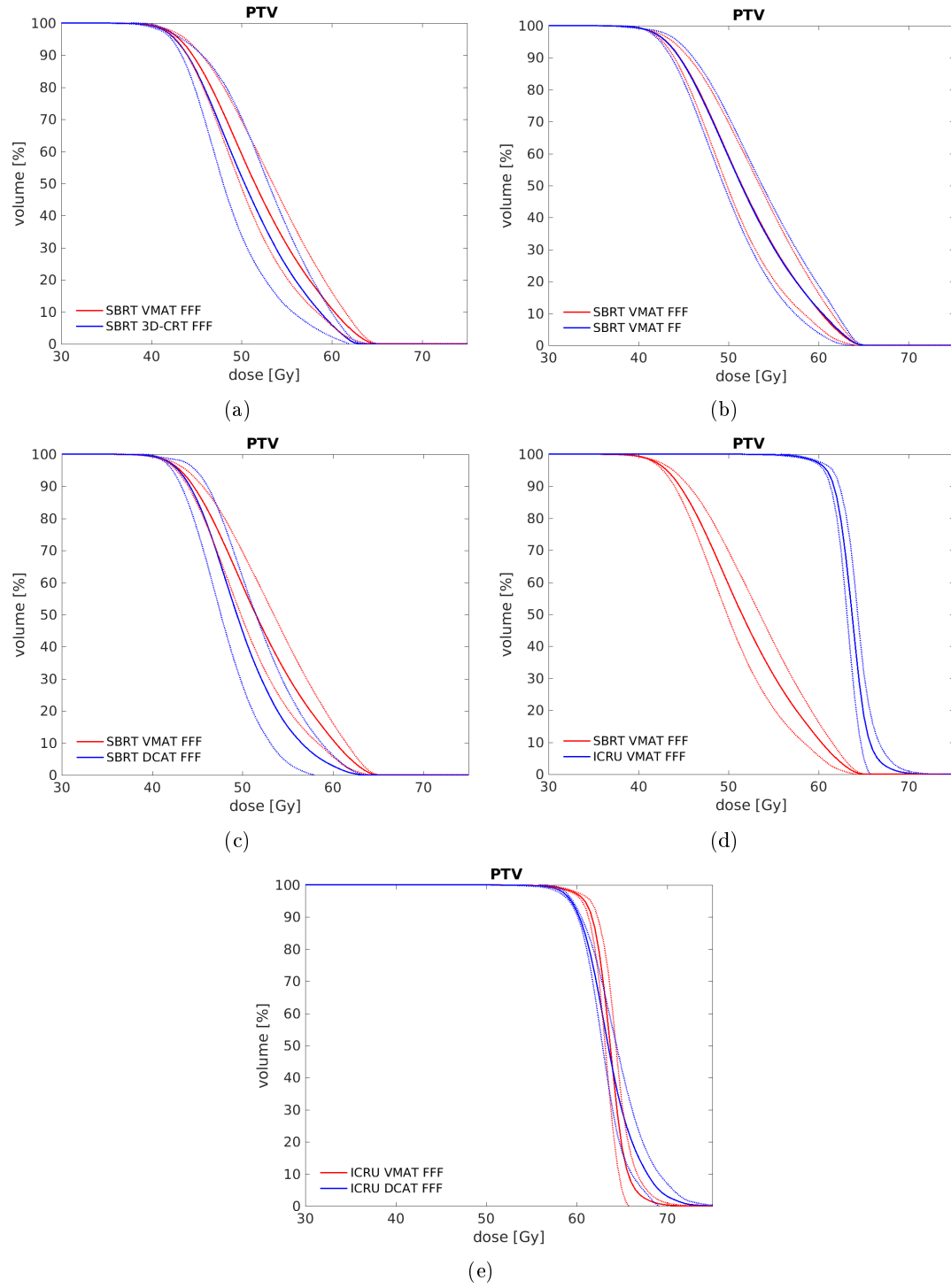
Figure 3.2: This figure shows dose-volume-histograms which were averaged over all patients. The continuous line illustrates the average whereas the dotted lines show the standard deviation. The first plot compares the unflattened SBRT VMAT plans with the clinically used 3D-CRT plans. The second one compares flattened and unflattened SBRT VMAT plans and the third plot compares the unflattened SBRT VMAT and DCAT plans. The last two plots compare unflattened ICRU and SBRT VMAT plans and unflattened ICRU VMAT and DCAT plans.

3.2 Measurement Preparation and Consistency Checks

The verification of the LINAC's output showed that the output of 200 monitor units using 6 MV flattened photon beams varied about 0.4 % (mean dose = 199.7±0.7 Gy), whereas the use of 10 MV reduced the output varriation to 0.3 % (mean dose = 199.1±0.5 Gy). Compared to that, the use of unflattened photon beams reduced the variation to 0.2 % for 6 MV (mean dose = 198.5±0.4 Gy) and 10 MV (mean dose = 198.0±0.4 Gy) beams. Due to the highest output variation of 0.4 %, the LINAC's output can be treated as stable. The average dose values of the output verification for seven days are shown in table 3.2.

Table 3.2: For the verification of the LINAC's output 200 monitor units, which equals 2 Gy, were irradiated to an ionization chamber. Following values are the mean values of the measurement days.

	6 MV FF [cGy]	10 MV FF [cGy]	6 MV FFF [cGy]	10 MV FFF [cGy]
day 1	199.4	199.0	198.9	198.0
day 2	199.5	199.0	199.0	198.1
day 3	200.0	199.2	198.3	197.6
day 4	200.3	199.3	198.4	198.1
day 5	200.8	199.8	199.0	198.6
day 6	199.3	199.1	198.0	197.4
day 7	198.9	198.3	198.2	197.9
mean	199.7	199.1	198.5	198.0
SD	0.7	0.5	0.4	0.4

In preparation for the measurements, a film calibration curve was recorded as already described in section 2.5. The parameters for the dose calculation were obtained through the calibration and are listed in table 3.3. Using these parameters, the dose values can be derived from the measured gray values.
The measured values and the fit curves for the dose channels and beam types are shown in figure 3.3.

Table 3.3: Parameter for the conversion of the netOD to dose [Gy]. Using equation 2.7 and the corresponding parameter depending on the beam type and the channel, the dose can be calculated.

| | FF | | FFF | |
	red channel	green channel	red channel	green channel
a	0.3711	0.4494	0.3295	0.5087
b	-8.377	-11.39	-9.731	-11.06
c	9.44e-05	0.0001522	5.063e-06	4.82e05
d	-34.19	-34.02	-42.4	-37.92

(a) Flattened Photon Beam - Green Channel   (b) Flattened Photon Beam - Red Channel

(c) Unflattened Photon Beam - Green Channel   (d) Unflattened Photon Beam - Red Channel
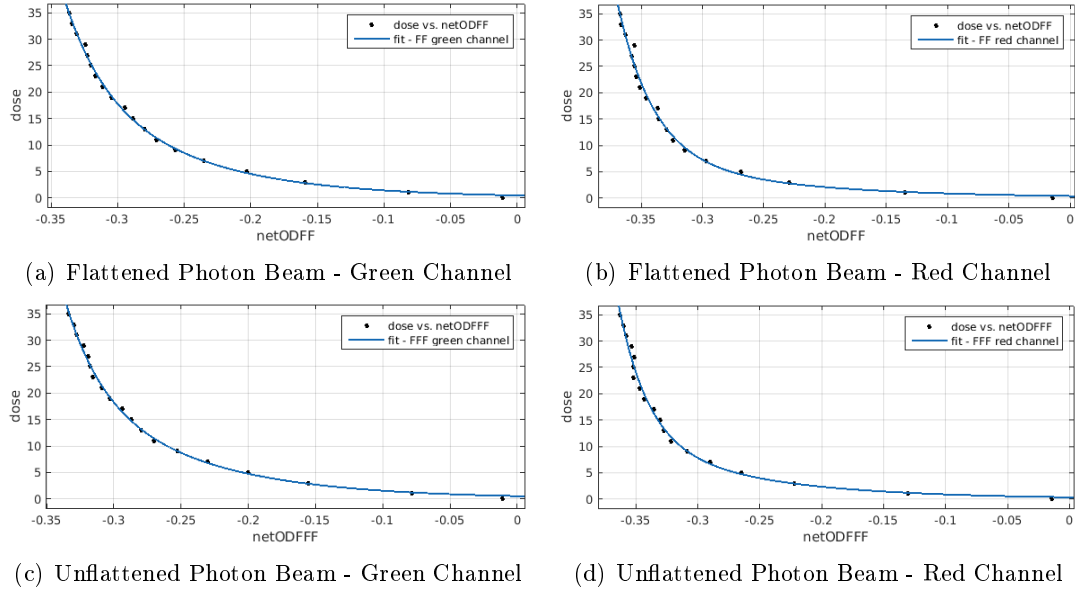
Figure 3.3: Fit functions for the film calibration. The black dots illustrate the measured values whereas the blue line illustrates the fitted function.

To evaluate the accuracy of the fit curves, the doses of the films which were used for calibration were calculated using the same process as used for the calculation of the other films. The comparison of the measured dose values and the actually radiated dose values showed differences of up to 9.6 % for the green channel (table 3.4)and up to 21 % for the red channel (table 3.5).

Table 3.4: Comparison of radiated and measured doses, calculated using the green channel.

ref. dose [Gy]	FF green channel		FFF green channel	
	meas. dose [Gy]	deviation [%]	meas. dose [Gy]	deviation [%]
15.0	15.1	0.8	14.8	-1.0
17.0	16.0	-5.6	16.1	-5.1
19.0	19.8	4.1	19.5	2.8
21.0	21.7	3.1	20.8	-1.0
23.0	25.2	9.6	24.6	7.0
25.0	25.1	0.2	24.5	-2.0
27.0	28.3	4.9	26.5	-1.9
	mean	2.4		-0.2
	STD	4.7		3.9

Table 3.5: Comparison of radiated and measured doses, calculated using the red channel.

ref. dose [Gy]	FF red channel		FFF red channel	
	meas. dose [Gy]	deviation [%]	meas. dose [Gy]	deviation [%]
15.0	16.2	8.0	14.7	-2.0
17.0	15.1	-11.1	14.9	-12.2
19.0	21.5	13.0	20.1	5.8
21.0	22.4	6.5	19.9	-5.0
23.0	27.8	21.0	25.8	12.1
25.0	24.8	-0.7	23.2	-7.1
27.0	30.1	11.4	25.8	-4.3
	mean	6.9		-1.8
	STD	10.3		8.2

Further consistency checks were done by comparing the mean dose values of some treatment plans irradiated without motion on two different days (table 3.6). Due to the higher dose rate and the resulting faster output, treatment plans for unflattened photon beams were used for the comparison.

The comparison showed deviations of up to 8 % and an average deviation of 3.6±5.7 % (excluding series four due to the significantly different values compared to the outer series).

Table 3.6: Consistency checks done by repeated measurements of unflattened treatment plans.

	treatment method	mean dose (without motion) [Gy]		deviation [%]
		first measurement	second measurement	
series 1	SBRT VMAT FFF	19.6	18.5	-5.5
	SBRT DCAT FFF	20.3	18.9	-6.8
series 2	SBRT VMAT FFF	18.3	19.7	7.5
	SBRT DCAT FFF	16.7	17.6	5.7
series 3	SBRT VMAT FFF	21.5	23.2	8.2
	SBRT DCAT FFF	19.2	19.9	3.8
series 4	SBRT VMAT FFF	22.9	19.3	-18.0
	SBRT DCAT FFF	19.5	16.5	-15.4
series 5[1]	SBRT VMAT FFF	21.1	22.3	5.8
	SBRT DCAT FFF	17.3	18.3	5.8
	ICRU DCAT FFF	23.5	25.5	8.1

[1] Repeated measurements executed on different LINACs.

As mentioned in section 2.7, the isocenter was shifted for the irradiation using longitudinal and realistic tumor motion. For the longitudinal tumor motion all plans were shifted 5 mm whereas the realistic tumor motion required different isocenter shifts. Measurement series one required a 5 mm shift, series two and three a 1 mm shift and series four and five stayed at the initial isocenter position. The comparison of the mean doses for the static plans with the isocenter at different positions showed a decrease of the mean dose of the 3D-CRT plan of -1.0±8.1%. In comparison, the SBRT VMAT plans exhibited an increase of the mean dose of 5.8±7.1% and 5.4±9.4% for unflattened and flattened beams, respectively. The other plans exhibited a smaller deviation between the different static positions, while all plans showed a high standard deviation.

Table 3.7: Mean dose values for static plans with a 5 mm isocenter shift. (Dose conversion was done using the green channel.)

| | FFF | | | FF | |
	3D-CRT [Gy]	SBRT VMAT [Gy]	SBRT DCAT [Gy]	SBRT VMAT [Gy]	SBRT DCAT [Gy]
static isocenter [Gy]	20.0±1.5	20.7±1.6	18.6±1.4	19,8±0.5	18.1±1.2
static 5 mm shift [Gy]	19.7±0.9	21.8±1.6	19.0±1.6	20.8±1.5	18.0±1.5
deviation [%]	-1.0±8.1	5.8±7.1	2.7±7.6	5.4±9.4	-0.7±5.9

| | FFF | | FF | |
	ICRU VMAT [Gy]	ICRU DCAT [Gy]	ICRU VMAT [Gy]	ICRU DCAT [Gy]
static isocenter [Gy]	22.8±1.6	22.7±0.9	21.7±1.5	21.5± 1.3
static 5 mm shift [Gy]	23.2±0.6	23.1±1.1	21.9±0.4	21.6±1.1
deviation [%]	1.6±6.7	2.3±5.7	1.7±5.7	1.0±7.1

3.3   Measurements Regarding the Interplay Effect

The main difference between flattened and unflattened photon beams is the increased dose rate and the resulting reduction of treatment time. Table 3.8 shows the beam-on time measured during the treatment without tumor motion for all measurement series and treatment methods.

The recorded beam-on time showed that the 3D-CRT plans allowed treatment almost twice as fast as VMAT plans. Furthermore, the recorded beam-on time showed that the use of unflattened treatment plans reduced the beam-on time by one third compared to flattened beams. Additionally, it can be seen that the beam-on time time for VMAT plans was increased compared to 3D-CRT and DCAT plans.

Table 3.8: Beam-on time recorded for all measurement series and treatment plans.

	FFF		FF	
3D-CRT [min:s]	SBRT VMAT [min:s]	SBRT DCAT [min:s]	SBRT VMAT [min:s]	SBRT DCAT [min:s]
01:47±00:07	03:30±00:42	01:49±00:18	10:19±02:39	05:38±00:49

	FFF		FF	
	ICRU VMAT [min:s]	ICRU DCAT [min:s]	ICRU VMAT [min:s]	ICRU DCAT [min:s]
	05:42±01:55	01:52±00:06	16:23±04:12	06:29±00:39

Table 3.11 represents the measured maximum, minimum and mean doses for the used tumor motions as well as for both channels. The color of the font refers to the used evaluation channel (the first mean, max and min doses correspond to the green channel, whereas the others correspond to the red channel).

Tukey's HSD test of the doses recorded without tumor motion, longitudinal tumor motion and realistic tumor motion showed no significant differences between the treatment plans for both channels.

Both channels led to variations in the measured doses: for example, the reduction of the mean dose of the static 3D-CRT plan, from 20.0±1.5 Gy to 18.8±1.6 Gy for the green and the red channel, respectively. However, the red channel also led to an increase of the dose as shown by the static maximum dose for the unflattened ICRU plan which increased from 29.5±2.8 Gy to 31.5±7.5 Gy for the green and red channel, respectively. The values of the standard deviation of the static mean and max doses for all plans showed average standard deviation values of 1.4 % and 2.4 % for mean and max dose of the green channel, and 3.4 % and 5.3 % for mean and max dose of the red channel. This increase of the standard deviation of the doses calculated with the red channel can also be observed for the other dose values.

In order to account for possible systematic errors due to variations in the measure-

ment setup and, additionally, for better comparability, the mean values in table 3.11 were standardized to the measured mean values of the static 3D-CRT treatment plans. These standardized mean values are shown in tables 3.9 and 3.10.

The normalized values for the 3D-CRT plan showed a decrease of the mean dose of 3 % for longitudinal and realistic tumor motion in comparison to the measurements without tumor motion. Furthermore, the maximum dose of the realistic motion was reduced by 2 % in comparison to longitudinal and without motion. In particular, the minimum dose was reduced by 8 % and 12 % for longitudinal and realistic motion, respectively. The unflattened SBRT VMAT plans exhibited a higher dose by 3 % for static and longitudinal motion and even 8 % higher for realistic motion compared to the static 3D-CRT plan. From this follows that the mean dose for realistic motion was increased by 5 % compared to the mean dose without motion. Additionally, the comparison of the maximum doses for unflattened SBRT VMAT plans showed an increase of the dose of 8 % for realistic tumor motion.

For the unflattened SBRT DCAT plans the dose was reduced for all motion types by 6 % and even 8 % for the static plans. Furthermore, the difference between the plans with realistic motion and without motion was reduced to 2 %, 3 %, and 3 % for mean, max, and min dose, respectively. The flattened SBRT VMAT plans exhibited a lower mean dose than the unflattened ones. However, the flattened SBRT VMAT plans showed an increase of the mean dose of 3 % and 7 % for longitudinal and realistic tumor motion compared to no tumor motion. Additionally, the maximum dose was increased by 6 % for realistic motion and the minimum dose was even increased by 7 % for realistic motion compared to no motion.

The flattened SBRT DCAT plans exhibited the lowest dose compared to the other SBRT plans. However, they showed hardly any differences between the motion types.

The evaluation of the ICRU plans (table 3.10) showed that the mean doses of the unflattened VMAT and DCAT were increased by 14 % in comparison to the SBRT 3D-CRT plans. The unflattened ICRU VMAT plans showed an increase of the mean dose by 6 % and an increase of the max dose by even 12 % between realistic motion and no motion. In contrast, the same comparison of flattened ICRU VMAT plans showed only an increase of 1 % and 7 % for mean and max dose, respectively. In contrast to the SBRT plans, the ICRU DCAT plans exhibited similar doses as the ICRU VMAT plans. However, the unflattened ICRU DCAT plan showed no difference between the mean dose of static and realistic motion and the difference for the max dose was only 2 %. In contrast, the flattened ICRU DCAT plans again showed an increase of 8 % and 4 % for the mean and max dose, respectively.

Furthermore, it has to be mentioned that the minimum dose of the ICRU plans was substantially increased compared to the 3D-CRT plans. The increase of the min dose for ICRU plans ranged from 18 % (ICRU VMAT FF) up to 28 % (ICRU VMAT FFF).

Table 3.9: Measured mean doses of all SBRT plans normalized to static values of the SBRT 3D-CRT plans.

| dose [Gy] | tumor motion | SBRT | | | | |
| | | FFF | | | FF | |
		3D-CRT	VMAT	DCAT	VMAT	DCAT
mean dose	static	1.00±0.00	1.03±0.06	0.92±0.02	0.99±0.06	0.91±0.05
	longitudinal	0.97±0.09	1.03±0.05	0.94±0.06	1.02±0.08	0.90±0.06
	realistic	0.97±0.04	1.08±0.04	0.94±0.06	1.06±0.07	0.91±0.04
max dose	static	1.00±0.00	1.09±0.11	0.94±0.03	1.06±0.06	0.88±0.04
	longitudinal	1.00±0.07	1.10±0.06	0.97±0.11	1.09±0.10	0.89±0.08
	realistic	0.98±0.05	1.17±0.08	0.97±0.06	1.12±0.10	0.91±0.06
min dose[1]	static	1.00±0.00	0.97±0.06	0.94±0.05	0.93±0.03	0.94±0.05
	longitudinal	0.92±0.12	0.95±0.03	0.91±0.06	0.94±0.07	0.91±0.08
	realistic	0.88±0.11	1.01±0.07	0.97±0.05	1.00±0.05	0.95±0.09

[1] Due to defects of the film the minimum doses were calculated using the 0.025 quantile.

Table 3.10: Measured mean doses of all ICRU plans normalized to static values of the SBRT 3D-CRT plans.

| dose [Gy] | tumor motion | ICRU | | | |
| | | FFF | | FF | |
		VMAT	DCAT	VMAT	DCAT
mean dose	static	1.14±0.07	1.14±0.08	1.08±0.05	1.07±0.05
	longitudinal	1.15±0.05	1.16±0.08	1.14±0.15	1.11±0.08
	realistic	1.20±0.08	1.14±0.05	1.09±0.10	1.13±0.05
max dose	static	1.16±0.09	1.14±0.09	1.09±0.05	1.06±0.06
	longitudinal	1.19±0.06	1.18±0.08	1.16±0.17	1.08±0.09
	realistic	1.28±0.12	1.16±0.05	1.16±0.13	1.10±0.08
min dose [1]	static	1.25±0.13	1.24±0.10	1.19±0.12	1.19±0.09
	longitudinal	1.23±0.03	1.26±0.05	1.23±0.16	1.22±0.08
	realistic	1.28±0.12	1.24±0.08	1.18±0.14	1.26±0.11

[1] Due to defects of the film the minimum doses were calculated using the 0.025 quantile.

Table 3.11: For the evaluation of the measured doses the maximum, minimum and mean dose values were compared for the red and green channel. Significant differences (p-value < 0.05) for the comparison of the measured doses of the generated treatment plans with the measured doses of the 3D-CRT plans were characterized using *. Highly significant differences were characterized by ** (p-value < 0.01).

| dose [Gy] | tumor motion | SBRT | | | | | ICRU | | | |
| | | FFF | | | FF | | FFF | | FF | |
		3D-CRT	VMAT	DCAT	VMAT	DCAT	VMAT	DCAT	VMAT	DCAT
mean dose	static	20.0±1.5	20.7±1.6	18.6±1.4	19,8±0.5	18.1±1.2	22.8±1.6	22.7±0.9	21.7±1.5	21.5± 1.31
	longitudinal	19.3±1.3	20.5±1.0	18.9±1.6	20.4±1.1	18.0±1.7	22.9±1.1*	23.1± 1.9**	22.6±1.6*	22.2±1.2
	realistic	19.3±1.3	21.5±1.2	18.8±1.7	21.1±1.2	18.3±1.6	24.0±1.9**	22.9±1.4*	21.8±1.7	22.6± 1.3
max dose	static	25.5±2.2	27.8±3.6	23.9±2.5	26.8±1.1	22.4±1.7	29.5±2.8	28.7±0.8	27.7±2.8	26.9±1.7
	longitudinal	25.4±0.9	27.8±1.7	24.5±2.6	27.7±1.8	22.6±2.5	30.3±1.4	30.0±2.8	29.2±3.1	27.5±2.3
	realistic	24.8±1.2	29.9±3.2	24.7±3.3	28.5±2.8	23.2±2.6	32.5±3.1**	29.4±2.4	29.3±3.1	27.7±2.0
min dose [1]	static	15.8±1.8	15.2±1.3	14.8±1.5	14.6±1.2	14.9±1.7	19.6±1.1**	19.3±0.9*	18.7±1.0	18.7±1.1
	longitudinal	14.7±3.1	15.0±2.1	14.4±2.3	14.9±2.1	14.4±1.8	19.3±1.8	19.9±2.1*	19.2±0.7	19.1±1.2
	realistic	14.06±2.9	15.9±2.0	15.3±1.8	15.9±1.9	15.0±1.5	20.0±1.9**	19.5±1.5*	18.4±1.1**	19.7±1.3**
mean dose	static	18.8±1.6	20.5±3.7	17.4±2.1	17.8±2.5	16.4±2.3	21.6±4.6	21.1±4.4	19.4±3.1	18.5±3.1
	longitudinal	16.99±3.5	18.2±3.3	16.8±1.6	17.8±2.1	15.2±1.6	19.6±2.5	20.4±3.0	18.2±2.5	18.8±2.7
	realistic	17.5±2.4	20.0±3.0	17.1±1.3	18.8±3.0	16.0±1.5	21.7±4.0	20.0±2.2	18.2±3.9	19.7±2.7
max dose	static	26.8±2.4	30.5±7.1	24.4±3.7	25.8±4.0	22.2±3.0	31.4±7.6	29.6±6.4	26.7±4.6	24.6±4.2
	longitudinal	25.3±4.1	27.3±5.7	24.5±3.3	26.5±3.4	20.5±3.0	28.5±5.5	27.9±4.3	25.2±3.0	25.4±4.2
	realistic	25.2±4.9	29.7±5.6	23.9±1.7	26.9±5.1	21.6±1.9	31.6±6.4	27.8±3.4	27.3±7.3	26.8±4.3
min dose [1]	static	14.3±1.2	14.5±2.1	13.2±1.1	12.7±1.3	13.0±1.7	17.7±3.5	17.3±3.5	16.2±2.4	15.5±2.4
	longitudinal	12.6±3.1	13.0±2.5	12.4±1.5	12.7±1.7	11.8±0.5	16.0±2.0	16.9±2.4	15.1±2.1	15.5±2.2
	realistic	12.2±1.8	14.1±1.5	13.3±0.9	13.7±1.6	12.6±0.7	17.4±2.6**	16.3±1.5	14.8±3.0	16.5±2.1

[1] Due to defects of the film the minimum doses were calculated using the 0.025 quantile.

Based on the mean values of table 3.11, the dose deviations between static and realistic tumor motion and, additionally, between static and longitudinal tumor motion, were calculated depending on tumor size. The deviations between the mentioned motion types are listed in table 3.12.

This table shows once more a reduction of the mean dose for realistic motion in comparison to no tumor motion for the 3D-CRT plan. However, the deviation was higher for smaller PTVs with a value of -6.1±7.8% instead of -1.6±2.3% for larger PTVs. The deviations of unflattened SBRT VMAT plans depending on target size were similar, with 3.7±2.3% and 4.7±4.0% for PTVs smaller and greater than 15.6 ccm. The flattened SBRT VMAT plans showed higher deviations than the unflattened plans, but the deviations of the unflattened plans were more or less similar for both target volumes, namely 6.2±8.6% and 6.8±6.2%.

The SBRT DCAT plans showed a variation of the deviations for the different target sizes of -0.4±4.3% and 2.7±4.4% for unflattened beams, and 5.8±4.6% and -2.1±5.1% for flattened beams.

The mean doses for ICRU VMAT plans were increased by 2.1±2.0% for smaller target volumes and increased by 7.2±2.8% for greater target volumes. The flattened ICRU VMAT and unflattened ICRU DCAT plans showed the same increase of the mean dose for both tumor sizes. For both planning methods, this evaluation showed a deviation of around 1%. Finally, the flattened ICRU DCAT plans again showed different deviation values for the different tumor sizes. The increase of the mean dose for small target volumes was measured as 9.0±2.8% and for larger target volumes as 2.7±4.7%.

Additionally, the mean values for static and longitudinal tumor motion are shown in table 3.12. The comparison again showed partially different values for the target sizes.

Table 3.12: Deviation of mean doses between motion types separated for target sizes.

| | PTV < 15.6 ccm | | PTV > 15.6 ccm | |
	static - real. deviation [%]	static - long. deviation [%]	static - real. deviation [%]	static - long. deviation [%]
3D-CRT FFF	-6.1±7.8	-9.1±13.8	-1.6±2.3	0.6±7.2
SBRT VMAT FFF	3.7±2.3	-4.4±7.2	4.7±4.0	2.3±5.1
SBRT VMAT FF	6.2±8.6	1.5±1.0	6.8±6.2	4.7±10.1
SBRT DCAT FFF	-0.4±4.3	-1.1±3.5	2.7±4.4	3.8±6.2
SBRT DCAT FF	5.8±4.6	8.5±9.2	-2.1±5.1	-6.6±6.9
ICRU VMAT FFF	2.1±2.0	-2.7±6.3	7.2±2.8	3.2±9.6
ICRU VMAT FF	0.5±2.7	11.2±3.4	0.6±8.1	1.0±3.1
ICRU DCAT FFF	1.1±1.5	-1.9±2.3	1.0±12.1	5.0±13.8
ICRU DCAT FF	9.0±2.8	6.9±3.5	2.7±4.7	1.7±6.0

Another comparison of the average dose values is shown in figure 3.5. It depicts all used treatment methods depending on the different motion types. The used doses for these plots were calculated using the green channel. This figure illustrates once again the significantly higher doses for all ICRU plans. Additionally, it can be seen that

the dose to the PTV for the static plans was similar or partially slightly higher using
SBRT VMAT plans instead of 3D-CRT plans. Nevertheless, the mean dose of the
SBRT DCAT plans was reduced compared to the static SBRT VMAT and 3D-CRT
plans. Furthermore, the boxplots in figure 3.5 illustrate that there are no substantial
differences between the mean dose values for the measurements with different tumor
motions. However, it shows a slight increase of the mean dose for SBRT VMAT plans
using realistic tumor motion, whereas the other doses were more or less constant. The
boxplots for the ICRU plans also showed an increase of the mean doses for VMAT plans
using realistic motion.

A detailed dose distribution within the irradiation field is shown in figure 3.4. These
plots illustrate the dose distributions across the radiochromic films. The comparison
of the film irradiated with and without tumor motion again showed no substantial
differences between the motion types.

The plots illustrate that no distinguishable differences between the measurements with
or without longitudinal tumor motion occurred. In comparison, the dose distribution
of the measurements with realistic tumor motion showed that the dose maximum was
partially shifted but not reduced due to tumor motion.

This can also be illustrated using the plots in figure 3.6. These plots show dose profiles
(calculated using the green channel) of the radichromic films for an unflattened SBRT
VMAT plan. Figures 3.6(a) and 3.6(b) illustrate the longitudinal and lateral dose
profile at the edge of the film (at 0 cm). Similarly, figures 3.6(e) and 3.6(f) illustrate
the opposite edges of the film (at 2.4 cm), whereas figures 3.6(c) and 3.6(d) illustrate
the middle layer (at 1.2 cm). The blue line represents the dose of the film irradiated
using realistic tumor motion. It can be seen that the plot of the longitudinal profile at
0 cm (figure 3.6(b)) represents a higher dose than the dose profile without tumor motion
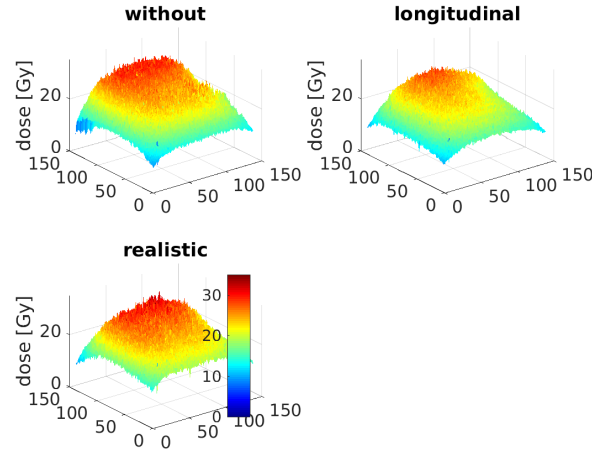(black line).

Figure 3.4: Comparison of the influence of the interplay effect to the dose distribution
depending on the tumor motion. This figure illustrates the dose distribution of an
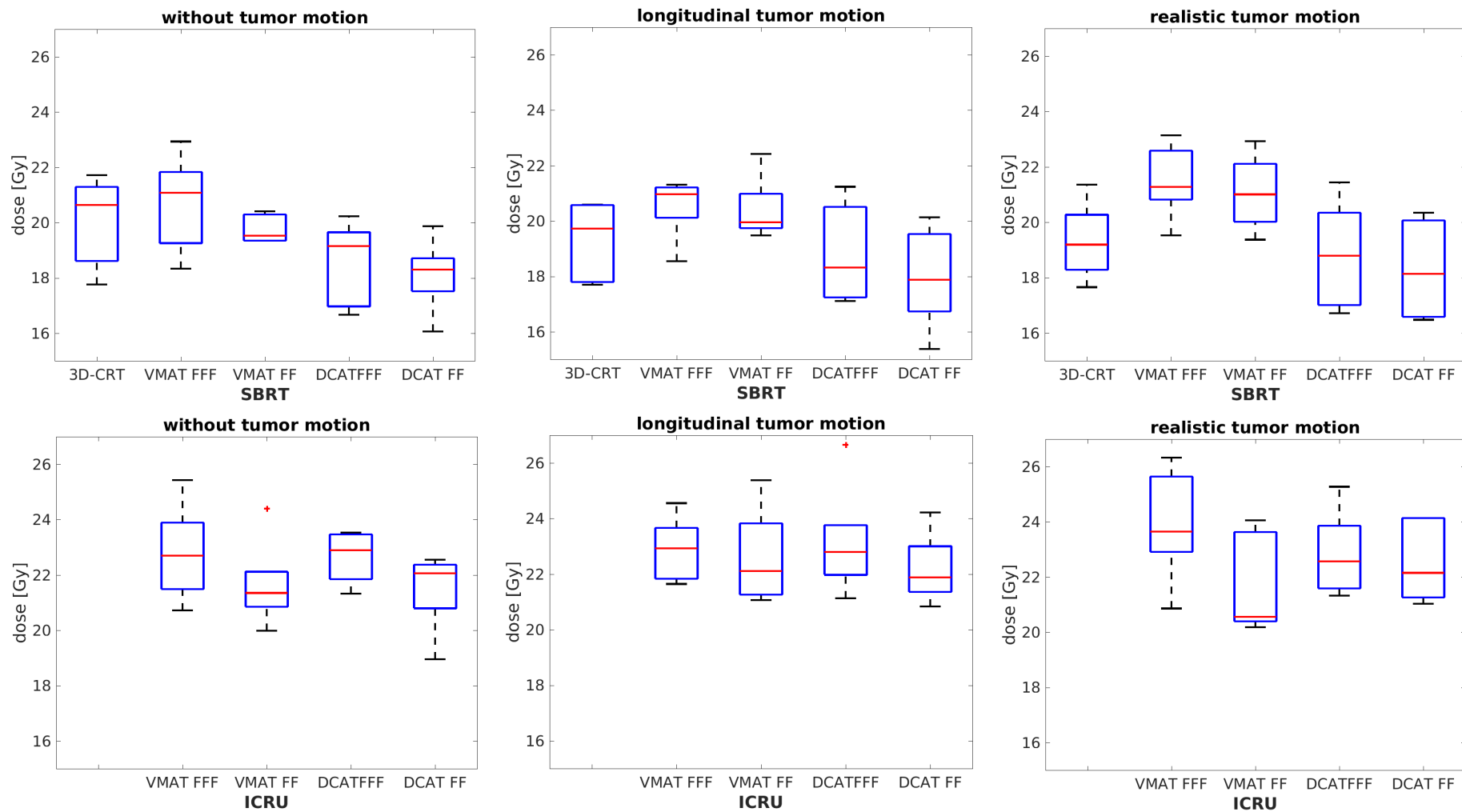unflattened SBRT VMAT plan.

Figure 3.5: Comparison of the measured mean doses for all treatment methods and motion types. For the conversion of the gray values to dose values the green channel was used.
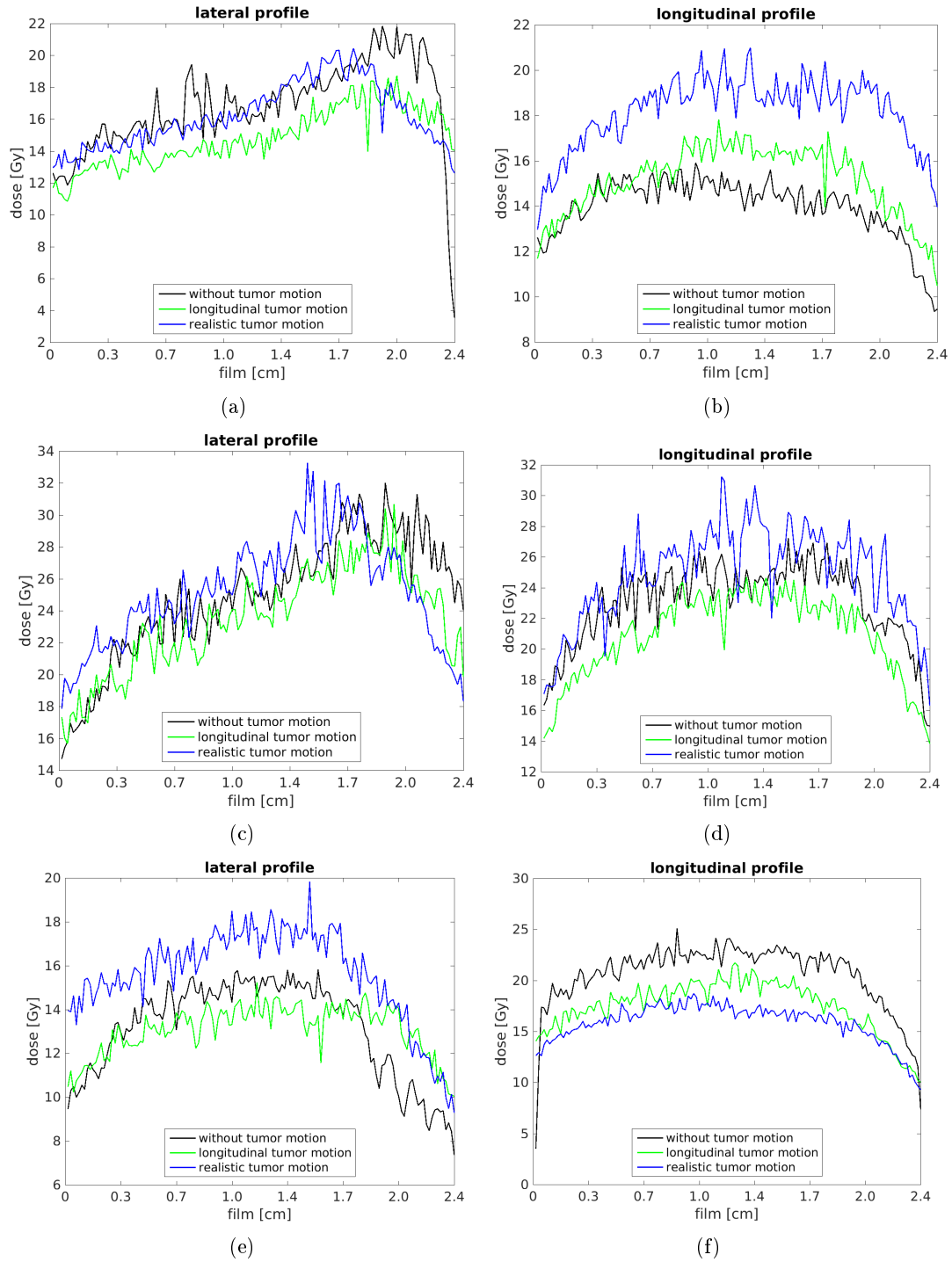
Figure 3.6: Measured dose profiles for an unflattened SBRT VMAT plan. The plots in the second row represent the dose profile 1.2 cm whereas the other plots represent the dose profiles at 0 cm and 2.4 cm.

3.4 Dose Calculation Accuracy

For the comparison of the measured and calculated dose distributions, the plans were recalculated using the phantom structure and the same properties as for the patient's plan. One example of the original patient plan and the recalculated plan is shown in figure 3.7. Due to the different structures and the smaller thorax, the recalculated dose within the PTV is higher than the dose to the PTV of the patient.
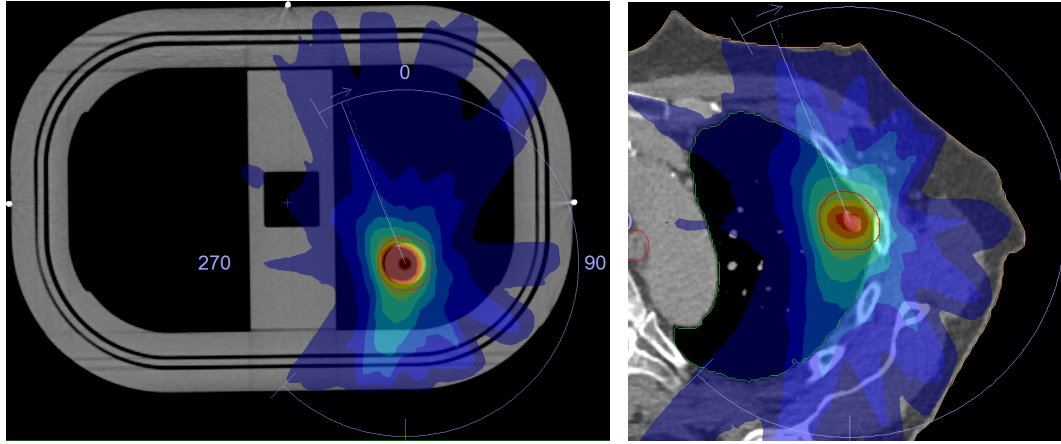
(a) Recalculated dose distribution for the phantom structure.

(b) Planned dose distribution for the patient.

Figure 3.7: A patient's SBRT VMAT FFF plan recalculated to the phantom structure for the evaluation of the treatment planning accuracy.

Due to the fact that the measured dose distribution specifies only a cutout of the calculated dose distribution, the matrices of the dose profiles were superposed to find the best matched area.

An example of matched dose profiles of an unflattened VMAT plan is shown in figure 3.8. The blue line illustrates the calculated dose profile, whereas the red line illustrates the measured dose profile. Figures 3.8(a) and 3.8(b) show the matched profiles of the dose distribution calculated using the green channel. They represent a good match for calculated and measured dose distribution. In contrast to that, figures 3.8(c) and 3.8(d) show a mismatch of the dose profiles which was caused by the lower dose calculated using the red channel.

The mismatch and the lower dose using the red channel can also be seen in figure 3.9(b). In comparison, figure 3.9(a) shows the dose distribution calculated using the green channel. It illustrates that the dose maximum was in the center of the film, and additionally, that the measured dose maximum and dose distribution were similar to the calculated ones.

In contrast to the first series, the second series exhibited a lower dose but without a dose shift for the green channel. However, the dose distribution of the ICRU plans was

shifted when the green channel was used. The third series, in turn, showed a lower dose and a dose shift when the red channel was used for the dose calculation. Series four and five did not show any dose shift for the use of the red channel; however, series four exhibited lower doses for the measured doses of some plans. In a similar manner, the fifth series exhibited higher measured doses for all plans when the red channel was used.
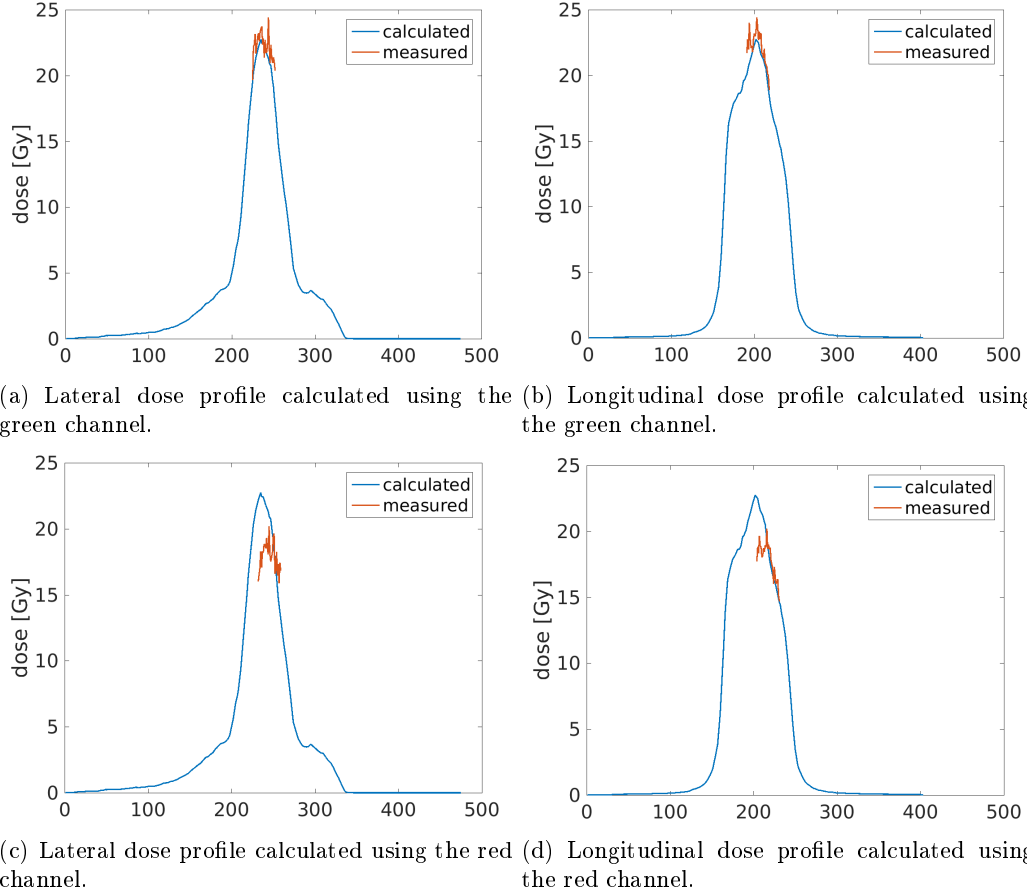

(a) Lateral dose profile calculated using the green channel.

(b) Longitudinal dose profile calculated using the green channel.

(c) Lateral dose profile calculated using the red channel.

(d) Longitudinal dose profile calculated using the red channel.

Figure 3.8: These plots show the measured (red line) and calculated (blue line) dose distribution. Plots a) and b) represent dose profiles which were calculated using the green channel, whereas plots c) and d) show dose profiles calculated using the red channel.
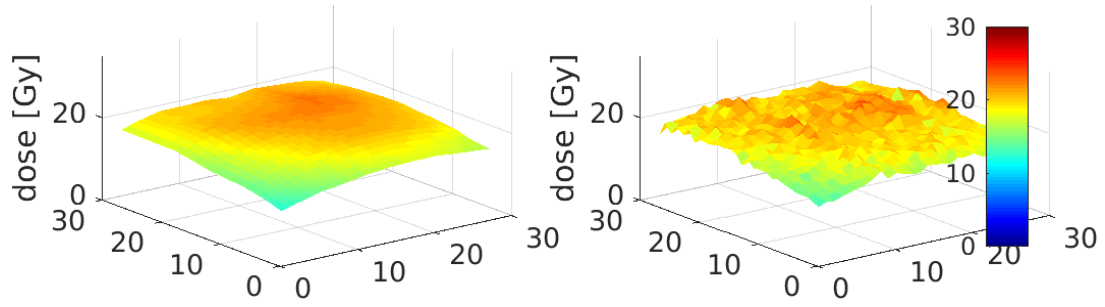
(a) Calculated (left) and measured (right) dose distribution evaluated using the green channel.
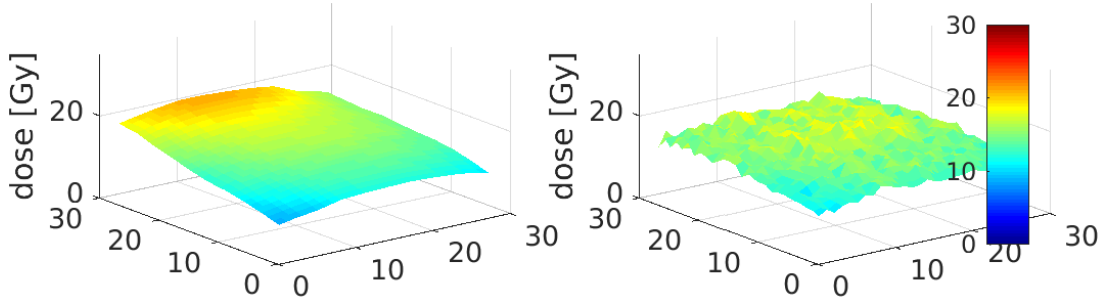
(b) Calculated (left) and measured (right) dose distribution evaluated using the red channel.

Figure 3.9: Comparison of the measured and calculated dose distributions using the red and the green channel for the conversion of the net optical density to dose [Gy].

A detailed comparison of calculated and measured doses is shown in table 3.13. This table lists the mean deviations calculated for each treatment method and measurement series, respectively.

The comparison showed variations in the deviations between measured and calculated mean doses. However, the average deviations of each series showed that a bigger PTV led to lower deviations of -0.1±1.0 % and -2.6±2.9 % for a target size of 62 ccm and 55 ccm, respectively. In contrast, the smaller target sizes of 9 ccm and 11 ccm led to a deviation of 6.2±3.6 % and -10.4±6.1 %. Furthermore, the target volume of 33 ccm led to a deviation of 4.1±1.1, which represents a deviation between the previously mentioned deviations.

Table 3.13: Mean deviations between calculated and measured doses.

	series 1^1 deviation [%]	series 2^2 deviation [%]	series 3^3 deviation [%]	series 4^4 deviation [%]	series 5^5 deviation [%]
SBRT VMAT FFF	-1.2±6.2	3.3±14.5	4.4±7.6	-21.2±17.6	-6.1±6.3
SBRT VMAT FF	0.2±5.2	1.8±21.3	5.1±11.8	-12.1±21.8	-1.6±8.2
SBRT DCAT FFF	-1.5±5.6	4.4±18.0	3.4±8.3	-16.9±9.8	0.0±4.5
SBRT DCAT FF	-0.8±4.5	7.8±14.2	4.9±5.0	-4.9±10.3	-6.9±5.3
ICRU VMAT FFF	0.2±5.2	6.5±14.8	2.9±6.0	-10.8±9.6	-4.7±5.6
ICRU VMAT FF	1.6±4.8	3.2±20.5	5.5±8.2	-5.1±9.6	-0.2±6.6
ICRU DCAT FFF	0.4±6.3	10.4±12.6	2.2±4.9	-7.8±7.1	-1.9±4.8
ICRU DCAT FF	0.7±5.1	11.8±18.8	4.1±7.1	-4.5±8.0	0.8±6.9
mean	-0.1±1.0	6.2±3.6	4.1±1.1	-10.4±6.1	-2.6±2.9

[1] PTV = 62 ccm
[2] PTV = 9 ccm
[3] PTV = 33 ccm
[4] PTV = 11 ccm
[5] PTV = 55 ccm

4 | Discussion

4.1 Dose Distribution

Target Coverage

The evaluation of the PTV coverage for all SBRT treatment plans showed that all generated treatment plans fulfilled the prescription to cover at least 99 % of the PTV with 65 % of the prescribed dose. However, the comparison of the conformity indices for 65 % of the prescribed dose showed that the VMAT plans provided best conformity in comparison to 3D-CRT and DCAT plans. This increase of conformity for VMAT plans was also reported by Ong et al. [48] and McGrath et al [39]. Additionally, the dose-volume-histogram which compared unflattened VMAT and 3D-CRT plans showed a slight increase of dose for the VMAT plans.
Due to the very significant reduction of the maximum dose for DCAT plans, the $CI_{80}\%$ exhibited a significant reduction compared to the other plans. Furthermore, the dose-volume-histogram illustrated a steeper dose fall-off and thereby a lower dose for the DCAT plans.
Similar to the study of Vassiliev et al. [65], the conformity indices and the dose-volume-histogram showed that no differences concerning the dose distribution occurred for flattened and unflattened treatment plans.
The evaluation of the ICRU plans showed a very significant increase of PTV and ITV doses compared to the SBRT plans. This is caused by the different dose prescriptions of the ICRU 83 report. The difference between the dose prescriptions can be shown using the conformity indices. While the SBRT plans showed their best conformity for the $CI_{65\%}$, the ICRU plans showed best conformity for $CI_{95\%}$. This results form the fact that the SBRT plans were designed to apply 65% of the prescribed dose to 99% of PTV, whereas the ICRU plans were planned to cover 98% of the PTV with 95% of the prescribed dose. The conformity indices of the ICRU plans for lower doses showed a decrease of conformity due to the fact that a high dose was applied to the lung outside the PTV. As a result of the lower dose prescription, this was not the case for the SBRT plans. The conformity indices $CI_{80\%}$ and $CI_{95\%}$ showed lower indices due to the fact that only some spots of the PTV reached these dose values. In contrast, the conformity indices $CI_{50\%}$ and $CI_{40\%}$ were reduced based on the dose application outside the PTV. Due to the ICRU 83 prescription of multiple dose-volume constraints including a pre-

scription for near-minimum, near-maximum and mean dose, the dose-volume-histogram for VMAT plans showed a substantially different dose-volume-histogram for ICRU and SBRT plans. The higher doses and the steeper dose fall-off for ICRU plans may lead to a reduction of the interplay effect. However, the dose conformity is very significantly reduced for all ICRU plans due to the higher prescribed doses. To avoid this clinically unacceptable dose conformity, a shift of the steep ICRU dose-curve to clinically used doses (as for example the SBRT dose) may improve treatment quality and could also compensate for interplay effects.

The ICRU report 83 prescribes to cover at least 98 % of the PTV with 95 % of the prescribed dose which equals a dose of 59.2 Gy. During treatment planning it became apparent that it was not possible to fulfill this prescription for DCAT plans using the Monaco system. Hence, the plans were planned using 95 % of the prescribed dose to a reduced volume of 95 % of the PTV. Thus, the dose-volume-histogram for DCAT plans showed a different dose-curve, starting with a lower near-maximum dose compared to ICRU VMAT plans. This is also the reason for the significant reduction of the dose coverage for the ICRU DACT plans.

Additionally, it was not possible to fulfill the prescription for the near-minimum dose which prescribes that 2 % of the volume are limited to 110 % of the prescribed dose (equals 68.5 Gy). This led to a significant increase of the near-minimum dose for ICRU DCAT plans in comparison to ICRU VMAT plans.

Organs at Risk

Despite the improved target dose, VMAT plans provided the lowest ipsilateral lung volume which received an EQD_2 dose of 20 Gy. Comparably, McGrath et al. [39] and Navarria et al. [43] reported a significant reduction of the dose to the lung for VMAT plans. Due to the use of Tukey's HST test, which considers multiple application of a statistical test on subgroups and a consideration of only eleven patients, the differences were not significant within this study. Looking at the ICRU plans a substantial difference of the ipsilateral lung dose between DCAT and VMAT plans can be seen.

Based on the fact, that for all treatment plans the irradiation through the contralateral lung was avoided, the volume receiving an EQD_2 dose of 5 Gy was minimal for all treatment plans.

The evaluation of all treatment plans showed that for all organs at risk the VMAT plans were characterized by the lowest doses compared to the other plans. The superior dose sparing to organs at risk for VMAT plans in comparison to 3D-CRT and DCAT plans was reported by Rauschenbach et al. [54] in the same way. Improved organ at risk sparing using VMAT can be applied due to the possibility of using intensity modulated beams in combination with the multi-leaf-collimator. However, the increased dose of the ICRU plans went along with higher doses to the organs at risk.

Similarly to the results reported by Vassiliev et al., the comparison of flattened and unflattened plans showed no differences concerning doses to organs at risk.

Monitor Units

As reported by McGrath et al. [39], Ong et al.[48], and Zhang et al. [69], the required number of monitor units for VMAT plans were very significantly increased. This increase of monitor units appeared in equal manner for flattened and unflattened VMAT plans and is caused by the higher degree of modulation using VMAT plans.

It has been observed that there are differences between monitor untis of flattened and unflattened treatment plans. However, these differences were not significant within this study due to the small PTVs and the dependence of this effect on PTV size (reported by Hrbacek et al. [26]).

A higher number of monitor units causes a higher surface dose, but, due to the fact that unflattened photon beams contain less contaminating electrons, the surface dose decreases for unflattened beams [11]. Thereby, higher monitor units for unflattened beams have less effect on the surface dose than flattened beams.

4.2   Treatment Time

The main improvement of unflattened photon beams is the increased dose rate and, thereby, the reduction of treatment time, as reported by e.g. Vassiliev et al. [66].

This study showed a decrease of beam-on time for unflattened VMAT and DCAT plans of approximately one third compared to flattened plans.

In contrast to the results of McGrath et al. [39], Ong et al. [48], and Navarria et al. [43] (the last group compared flattened 3D-CRT with unflattened VMAT), which stated a reduction of treatment time for VMAT plans compared to 3D-CRT plans, this study showed a near doubling of the beam-on time for VMAT plans compared to 3D-CRT and DCAT plans.

Even if the gantry rotation, which is estimated to around 1 min, is added to the beam-on time, the 3D-CRT will allow a shorter treatment time. This resulted especially from the occurrence of a so-called "Dose rate mon" error during unflattened VMAT delivery which stopped the irradiation (measurement of beam-on time was stopped if the error occurred). Despite these errors, the LINAC allowed to continue the irradiation after a reset of the machine. Simultaneously, the phantom motion continued, which may have led, besides the increased treatment time, to a modification of the dose to the target. Due to the fact that there are no significant differences between flattened and unflattened VMAT plans, the effect of the interruption of the treatment on the dose distribution was assumed to be negligible. The occurrence of this error could be avoided if a fine tuning of the machine would be done.

Due to the fact, that the 3D-CRT reduced planning and beam-on time in comparison to VMAT plans, and the fact that there are no significant differences for OARs, the implementation of VMAT plans for clinical use may be abdicable. The unflattened DCAT plans showed a similar beam-on time to the 3D-CRT plans, but, as already mentioned, the dose conformity and organ sparing was reduced for DCAT plans. For this reason the clinical use would reduce the treatment quality.

4.3   Film Dosimetry

The comparison of calculated and measured doses in the relevant dose range showed substantial differences between the doses calculated by the use of the red and green channel. The mean deviations for doses calculated using the green channel exhibited a lower mean deviation than the mean deviation for the red channel.

Similarly to these results, Borca et al. [7] reported that the red channel provides the best response of up to 10 Gy, whereas for doses higher than 10 Gy the green channel has a greater response. Besides this, Papaconstadopoulos [51] suggested a scanning protocol for reflection scanning of EBT3 films using the red channel for doses less than 2 Gy, and the green channel for higher doses.

Further evidence for the better use of the green channel is the fact that the matching of the calculated and measured dose matrices showed better results for the matching of the doses calculated using the green channel. The use of the red channel led to a partial shift of the measured dose maximum in comparison to the calculated one.

The plots (figure 4.1) illustrate the measured net optical densities for known doses of 9 Gy and 21 Gy (and additionally 25 Gy for the green channel) for flattened and unflattened photon beams, respectively. Due to the high gradient of the fit curve, a small difference in the measured net optical density led to a high difference of the calculated dose. As shown in 4.1(a), the influence of different net optical densities had a substantial higher effect to the dose for the radiation of 21 Gy than for 9 Gy. As it can be seen in figure 4.1, the dose for the radiation of 21 Gy covered a dose range of 21.6 Gy to 24.6 Gy, whereas the dose range for 9 Gy was 9.2 Gy to 10 Gy.

In contrast, the dose calculated using the green channel is shown in figure 4.1(b). The illustration shows once more that the dose gradient of the fit curve influences the dose values, but, due to the smaller dose gradient compared to the red channel, the influence was smaller. However, the use of the green channel also led to a higher difference of the calculated dose for higher radiated doses. The green channel reduced the dose range for 9 Gy to 9.1 Gy up to 9,5 Gy. Especially for higher doses, such as 21 Gy, the dose range was reduced to 21.4 Gy up to 22.4 Gy.

However, this is still a high variation. Due to the fact that the used film had its optical dose range between 0.2 Gy and 10 Gy, the use of radiochromic films, which are more stable in the used dose range, would improve measurement accuracy. New films with an extended dose range are in principle commercially available, but were not available in the institution at the time this study was performed.

Due to the fact that the net optical density is sensitive to dose, the time between irradiation and scanning can distort the results caused by the darkening of the film in the first hours after the irradiation. However, since the scanning was done approximately 48 hours after the irradiation, this effect should be negligible.

Repeated measurement of some static plans showed substantial differences between the mean doses. These differences were caused by the high gradient of the fit curve and the resulting influence of the net optical density to dose. Based on these measurements, the uncertainty of measurement was estimated to be around 5%.
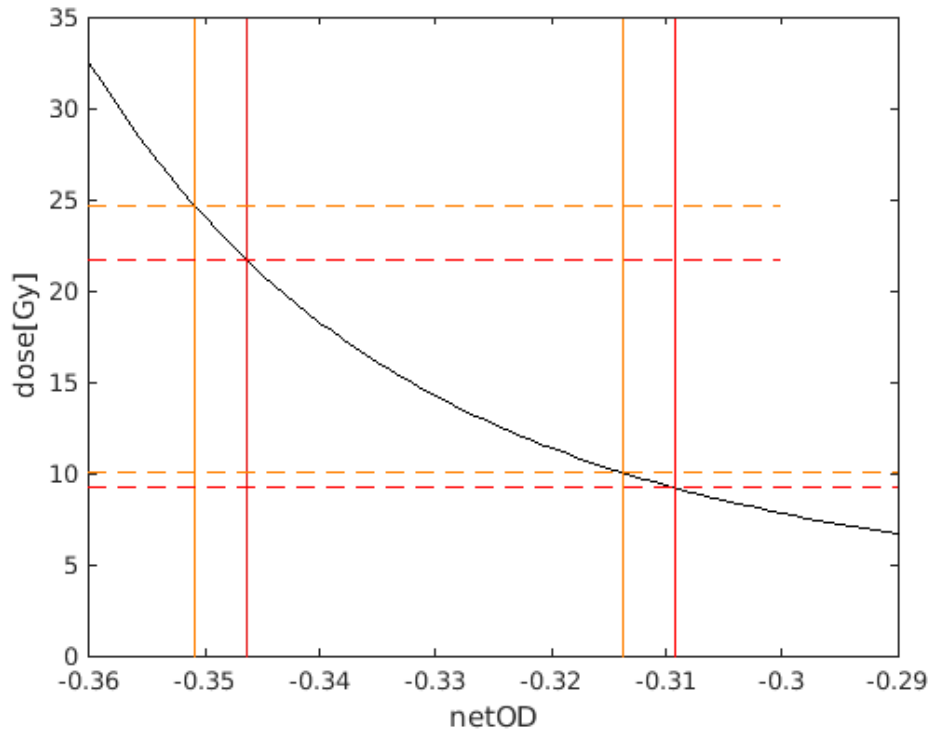
(a) red channel - plotted are the measured netOD for 9 Gy and 21 Gy
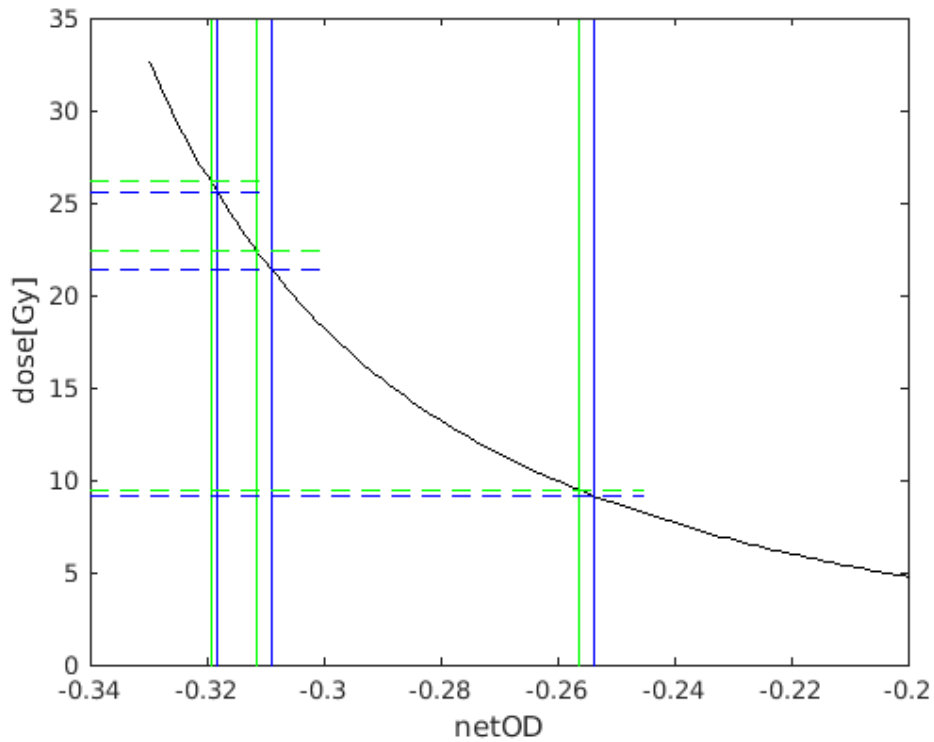
(b) green channel - plotted are the measured netOD for 9 Gy, 21 Gy, and 25 Gy

Figure 4.1: Illustration of the influence of the fit curve's gradient on the dosimetric accuracy.

4.4   Interplay Effect

The comparison of the measured mean values for the different treatment plans in combination with different tumor motions showed no significant differences, aside from some significant increases of the dose for the ICRU plans due to the higher prescribed dose. The normalization to the static 3D-CRT revealed that no systematic errors due to inaccurate phantom positioning occurred. However, these values showed an increase of 5 % to 8 % for the mean and max doses of flattened and unflattened VMAT plans using realistic tumor motion instead of no motion. These values are similar to the results of Tyler et al. [63] and Ong et al. [47, 49] who reported a deviation for VMAT treatment of 2% to 5% (respectively, the use of single arcs and/or single fractions induced deviations of 7.4% to 9.4%).
Furthermore, the measured deviations of mean and maximum doses for unflattened DCAT plans showed a difference of 2 % to 3 % whereas the flattened DCAT plans showed no substantial deviation. Similarly, the deviation of mean and max doses for 3D-CRT were around -3 % to -2 % which, due to an uncertainty of measurement of 5%, is more or less related to the study of Tyler et al. [63]. It reported that 3D-CRT treatment is largely unaffected by target motion due to the static beam delivery.
The ICRU plans showed high variations in the deviation between mean and max doses for realistic tumor motion and no tumor motion. This is probably caused by the higher doses for ICRU plans and the higher measurement uncertainty for higher doses.
Furthermore, the deviations between the different motion types were calculated for PTVs larger than 15.6 ccm and PTVs smaller than 15.6 ccm separately. These values showed substantial differences and variations between the different plans and target sizes. This can be caused, on the one hand, by the uncertainty of measurement of 5 % and, on the other hand, by the fact that only two or, respectively, three values are used for the calculation of the mean value. A larger data set may lead to a more specific result.
The box plots of the different treatment plans still showed substantial differences between the different treatment plans due to their varying dose prescriptions. Furthermore, slight differences between static and realistic motion can be seen for flattened and unflattened VMAT plans but this difference was not statistically significant.

It has to be mentioned that the phantom used in study did not allow the determination of its starting position. Thereby, it was not possible to regulate the position of the tumor at the beginning of the treatment which can cause differences in the dose to the target due to the interplay effect. This resulted in variations of the dose to the target, especially for the irradiation using separate beams. Considering the errors which occurred during the irradiation of VMAT plans and stopped the treatment, this can cause variations of the target dose. This is also the case for patient treatment, but, nevertheless, it can be a reason for dose deviations.
Furthermore, the partial shift of the isocenter led to different doses to the target due to the variation of the thickness of the phantom's thorax. The comparison of the mea-

sured doses for static irradiation at the isocenter and the irradiation with a 5 mm shift exhibited a dose deviation of up to 5.8±7.1 %.

To sum up, the results concerning the interplay effect lead to the conclusion that no significant differences between the different motion types occurred for any of the treatment plans. Due to the uncertainty of measurement of around 5 %, the interplay effect can be estimated not to significantly exceed the measurement uncertainty. Furthermore, the measurement showed that the used film was not suitable for this dose range despite its dynamic dose range of up to 20 Gy. The use of a new type of film which is more suitable for the used dose range may lead to a more precise evaluation of the influence of the interplay effect.

4.5   Dose Calculation Accuracy

The comparison of the calculated and measured mean doses showed substantial differences. Compared to the other deviations, the higher deviation for the PTV sizes of 9 ccm and 11 ccm is remarkable. The higher deviations for the smaller target volumes may be caused by dosimetric effects which occur in small fields and cause errors and uncertainties of measurements and dose delivery. Furthermore, the uncertainty of measurement of 5 % increases the deviations for all target sizes. The LINAC's calibration can be excluded as reason for the deviation since it was shown to be stable within 1 %. Once more, the use of films suitable for higher dose ranges can reduce the deviation between measured and calculated doses.

5 | Conclusion and Outlook

The SBRT VMAT plans generated with the treatment planning system Monaco 5.00.04 (Elekta AB, Stockholm, Sweden) allowed best dose conformity and OAR sparing compared to the clinically used SBRT 3D-CRT and the SBRT DCAT plans. However, this went along with a very significant increase of the used monitor units for the SBRT VMAT plans which, thereby, increases the surface dose. In the same context, the SBRT DCAT plans showed worst dose conformity and higher doses to the OARs.

Due to the higher prescribed doses for the ICRU plans these plans exhibited more dose to the OARs for VMAT and DCAT plans. Especially, the ICRU DCAT plans exhibited particularly high doses for the OAR which were partially not clinically acceptable . Additionally, due to the higher doses, conformity was worse compared to the SBRT plans, making the ICRU plans clinically unacceptable. However, the ICRU plans showed a dose-curve with a steeper dose fall-off which could, when shifted to lower doses, improve treatment quality due to a reduction of the interplay effect.

For both dose prescriptions and all treatment plans the use of flattened and unflattened photon beams showed no differences concerning dose coverage, dose conformity and doses to OARs. The main improvement was the substantial reduction of the beam-on time for unflattened photon beams.

Contrary to prior expectations, the recorded beam-on time for all treatment plans showed that the unflattened 3D-CRT plans allowed shortest beam-on time, followed by unflattened DCAT plans. The unflattened VMAT plans showed a higher beam-on time due to the increased number of required monitor units.

The evaluation of the measurements showed that in the used dose range of 15 to 27 Gy the film dosimetry using the green channel provided better results than the red channel. Nevertheless, despite the dynamic dose range of the EBT3 films of up to 20 Gy, the uncertainty of the measurements came to around 5 %.

No significant differences concerning mean, maximum and minimum doses were observed for the treatment plans measured with longitudinal tumor motion, realistic tumor motion and without tumor motion. However, a detailed evaluation of the mean doses showed a reduction of the mean dose of 2-3 % for unflattened clinically used 3D-CRT plans for realistic tumor motion compared to the measurement without tumor motion. Similar to that, the flattened and unflattened DCAT plans showed an increase of the mean dose of 2-3 % when realistic tumor motion was used. In contrast to that, the unflattened and flattened VMAT plans exhibited an increase of the mean dose of 5-7 %.

Due to the higher doses, the deviations of the ICRU plans showed high variations, which is why no deviation factor was defined.

Considering the uncertainty of measurement it can be said that the influence of the interplay effect was not significantly higher than the measurement uncertainty.

To put it in a nutshell, the 3D-CRT treatment plans allowed the shortest beam on-time and the lowest influence of the interplay effect. Due to an insignificant level of improvement concerning dose conformity and OAR sparing in addition to the highly significant increase of MU for VMAT plans, the unflattened 3D-CRT treatment method is still a good choice for clinical use.

For a more accurate evaluation of the influence of the interplay between target motion and MLC motion, measurements using films which are more suitable for the used dose range need to be performed. This would result in a more precise value for the deviation of the dose between different treatment plans. Additionally, these measurements might potentially show the influence of flattened and unflattened photon beams on the interplay effect.

Furthermore, the use of an ionization chamber, which enables the measurement of the absolute dose in the isocenter, would allow for comparison between the dose measured using the film and the ionization chamber (the phantom has an insert for ionization chambers, as well). This would then allow an estimation of correction factors for the film. However, measurements in steep dose gradients exhibit considerable uncertainties which may complicate the determination of the correction factors. Additionally, the influence of the phantom's 5 mm isocenter shift can be measured more accurately and a correction factor can be determined. The measurements showed that for this isocenter shift a precise alignment is also essential.

In addition, the possibility of determining the phantom's motion starting position would allow the evaluation of the influence of the interplay effect on the different treatment methods in a more detailed way.

A | Monaco TPS

A.1 Lung Templates

The main improvement of the Monaco treatment planning system (TPS) is the possibility of using templates which provide a basis for all treatment plans. Once a template for the required treatment plan is created, it can be used for other patients. Only the gantry angle has to be adjusted for every patient before the first optimization can be started.

After the first optimization, which takes around 10 minutes, the isoconstraints can be adapted to the individual plan. Then the second optimization, which takes between 30 and 45 minutes, can be started. The treatment plan can be furhter improved after the second optimization by adapting the isoconstraints. The second optimization steps can be repeated as often as necessary and only take a few minutes.

A.1.1 Template for Volumetric Modulated Arc Therapy

The cost functions for the VMAT templates were chosen as shown in table A.1. In this table the cost functions for the OARs are those for the SBRT dose prescription. For ICRU plans the isoconstraints for the OARs had to be eased.

For some plans it was useful to additionally use the quadratic overdose function for the healthy side of the lung or the heart to reduce the maximum dose.

Table A.1: Template for VMAT plans.

Structure	Cost Function	Additional Parameter	Reference Dose [Gy]	Isoconstraint
PTV	Target EUD[1]	Cell Sensitivity: 0,50 Surface Margin: On		Prescription [Gy]: 40.500
	Quad. Overd.[1]		Max. Dose: 65.00	RMS [Gy]: 0,020
	Target EUD[2]	Cell Sensitivity: 0,50 Surface Margin: On		Prescription [Gy]: 59.2
	Overd. DVH[2]		Obj. Dose: 66.66	Max. Vol: 2 %
	Underd. DVH[2]		Obj. Dose: 59.20	Min. Vol: 98 %
Lung right	Parallel	k: 2.00	Ref. Dose: 13.400	Mean Organ Damage [%]: 10.00
Lung left	Parallel	k: 2.00	Ref. Dose: 13.400	Mean Organ Damage [%]: 10.00
Heart	Serial	k: 6.00		EUD [Gy]: 7.000
Stomach	Serial	k: 5.00		EUD [Gy]: 5.000
Myelon	Serial	k: 14.00		EUD [Gy]: 6.000
Esophagus	Serial	k: 12.00		EUD [Gy]: 6.000
Body	Quad. Overd.		Max. Dose: 30.000	RMS [Gy]: 0.800
	Quad. Overd.		Max. Dose: 39.800	RMS [Gy]: 0.050
	Quad. Overd.		Max. Dose: 20.000	RMS [Gy]: 1.200

[1] These functions are used for SBRT VMAT plans.

[2] Cost functions for the VMAT plans generated using multiple dose-volume constraints (ICRU Report 83).

A.1.2   Template for Dynamic Conformal Arc Therapy

The used cost functions for the dynamic conformal arc template are listed in table A.2. To comply with the PTV coverage prescriptions, the angle range was irradiated twice (clockwise and counterclockwise) for almost all plans. For the template a collimator angle of 90° was chosen because this provided better results for most of the plans. However, for some plans it was necessary to change the collimator angle to 5° to reach the specified values.
Additionally, the *Target Margin* had to be adjusted to *Very Tight* to reach a better conformity. For ICRU plans the isoconstraints for the OARs had to be eased.

Table A.2: Template for DCAT plans.

Structure	Cost function	Additional parameter	Reference dose [Gy]	Isoconstraint
PTV	Target Penalty[1]	Min. Vol.[%]: 99,00 Surface Margin: On		Prescription [Gy]: 40,500
	Quad. Overd.[1]		Max. Dose: 65,00	RMS [Gy]: 0,020
	Target Penalty[2]	Min. Vol.[%]: 95,00 Surface Margin: On		Prescription [Gy]: 59.2
	Overd. DVH[2]		Obj. Dose: 66.66	Max. Vol: 10 %
	Underd. DVH[2]		Obj. Dose: 59.20	Min. Vol: 95 %
Lung right	Parallel	k: 2,00	Ref. Dose: 13,400	Mean Organ Damage [%]: 10,00
Lung left	Parallel	k: 2,00	Ref. Dose: 13,400	Mean Organ Damage [%]: 10,00
Heart	Serial	k: 6,00		EUD [Gy]: 9,000
Myelon	Serial	k: 14,00		EUD [Gy]: 7,000
Esophagus	Serial	k: 12,00		EUD [Gy]: 7,000
Body	Quad. Overd.		Max. Dose: 30,000	RMS [Gy]: 1,00
	Quad. Overd.		Max. Dose: 39,800	RMS [Gy]: 0,100
	Quad. Overd.		Max. Dose: 20,000	RMS [Gy]: 1,500

[1] These functions are used SBRT DCAT plans.
[2] Cost functions for the DCAT plans generated using multiple dose-volume constraints (ICRU Report 83).

List of Acronyms

3D-CRT Three-dimensional conformal radiation therapy

BED biological effective dose

CBCT cone beam computed tomography

CI conformity index

CT computed tomography

CTV clinical target volume

DCAT Dynamic conformal arc therapy

DVH dose-volume-histogram

EBRT external beam radiation therapy

EUD equivalent uniform dose

EQD$_2$ equivalent uniform dose in 2 Gy fractions

FF flattening filter

FFF flattening filter free

GTV gross tumor volume

HSD honestly significant difference

ITV internal target volume

LINAC linear accelerator

MC Monte Carlo

MLC multi-leaf-collimator

MU monitor units

PTV planning target volume

OAR organ at risk

RF radio frequency

ROI region of interest

SBRT stereotactic body radiation therapy

TPS treatment planning system

VMAT Volumetric modulated arc therapy

List of Figures

List of Tables

Selbständigkeitserklärung

Ich, Marie-Theres Bsteh, bestätige hiermit, die vorliegende Arbeit selbstständig verfasst und keine anderen als die angegebenen Quellen und Hilfsmittel verwendet zu haben. Diese Arbeit wurde bisher in keiner Form einer anderen Prüfbehörde vorgelegt und auch nicht veröffentlicht.

_____

Wien, 20.Oktober 2016

Bibliography

[1] Abdi H, Williams L, Tukey's Honestly Significant Difference (HSD) Test, In Neil Salkind (Ed.), Encyclopedia of Research Design, Thousand Oaks, CA: Sage, 2010

[2] Aigner H, Poljanc K, Frank B, Kaska K, Kragl G, Richter H, Skriptum Teilchenbeschleuniger (Vorlesung 141.944), Atominstitut der Österreichischen Universitäten, 2005

[3] American Association of Physicists in Medicine, The Management of Respiration Motion in Radiation Oncology, AAPM Report No 91, Report of AAPM Tast Group 76, 2006

[4] American Cancer Society, http://www.cancer.org/ (8th May 2016)

[5] Ashland Medical Dosimetry, Gafchromic Dosimetry Media, Type EBT-3, http://www.gafchromic.com/gafchromic-film/radiotherapy-films/EBT/index.asp (16th August 2016)

[6] Bailey D, Humm H, Todd-Pokropek A, van Aswegen A, Nuclear Medicine Physics: A Handbook for Teachers and Students, Vienna: International Atomic Energy Agency, 2014

[7] Borca V, Pasquino M, Russo G, Grosso P, Cante D, Sciacero P, Girelli G, La Porta M, Tofani S, Dosimetric characterization and use of GAFCHROMIC EBT3 film for IMRT dose verification, Journal of Applied Clinical Medical Physics, Vol 14 (2), 2013, DOI: 10.1120/jacmp.v14i2.4111

[8] Brainlab, Monte Carlo Dose Algorithm, Clinical White Paper

[9] Chand D, Lasley F, Das I, Mendonca M, Dynlacht J, Basic Raiotherapy Physics and Biology, Spinger 2014, DOI: 10.1007/978-3-319-06841-1

[10] Christian Doppler Laboratory for Medical Radiation Research for Radiation Oncology, New Linac "Versa HD" at the Department of Radiation Oncology, MUW, www.meduniwien.ac.at/radonc (11th March 2016)

[11] De Puysseleyr A, Lechner W, De Neve W, Georg D, De Wagter C, Absorbed dose measurements in the build-up region of flattened versus unflattened megavoltage photon beams, Zeitschrift für Medizinische Physik, Vol 26 (2), 177-183, 2016, DOI: 10.1016/j.zemedi.2016.02.005

[12] Demtröder W, Experimental Physik 1 - Mechanik und Wärme, Fünfte, neu berbeitete und aktualisierte Auflage, Springer 2008, DOI: 10.1007/978-3-540-79295-6

[13] Demtröder W, Experimental Physik 3 - Atome, Moleküle und Festkörper, Dritte, überarbeitete Auflage, Springer 2009, DOI: 10.1007/978-3-642-03911-9

[14] Demtröder W, Experimental Physik 4 - Kern-, Teilchen- und Astrophysik, Vierte, überarbeitete Auflage, Springer 2010, DOI: 10.1007/978-3-642-01598-4

[15] Department of Radiotherapy and Radiation Oncology, University Clinic Mannheim, Ruprecht-Karls-Universität Heidelberg, Medical Faculty Mannheim at Heidelberg University, Flattening filter free (FFF) Linac, http://www.radiation-oncology.de/index.php?page=flattening-filter-free-linac (7th September 2016)

[16] Devic S, Seuntjens J, Sham E, Podgorsak E, Schmidtlein R, Kirov A, Soares C, Precise radichromic film dosimetry using a flat-bed document scanner, Med Phys, Vol 32 (7), 2245-2253, 2005, DOI: 10.1118/1.1929253

[17] Elekta, Monaco 5.00 Training Guide, Document ID: LTGMON0500, Part Number: C#98961-E

[18] Elekta, Versa HD - The convergence of conventional radiotherapy with advance stereotactic precision., Versa Hd Brochure Dec 9 2014 marketinginfo

[19] Fippel M, Haryanto F, Dohm O, Nuesslin F, Kriesen S, "A virtual photon energy fluence model for Monte Carlo dose calculation, Med Phys, Vol 30 (3), 301-311, 2003, DOI: 10.11118/1.1543152

[20] Fleckenstein J, Hesser J, Wenz F, Lohr F, Robustness of sweeping-window arc therapy treatment sequences against intrafractional tumor motion, Medical Physics, Vol 42 (4), 1538-1545, 2015, DOI: 10.1118/1.4914166

[21] Gasic D, Ohlhues L, Brodin P, Fog L, Pommer T, Bangsgaard J, Munck af RosenschÃűld P, A treatment planning and delivery comparison of volumetric modulated arc therapy with or without flattening filter for gliomas, brain metastases, prostate, head/neck and early stage lung cancer, Acta Oncologica, Volume 53, 1005-1011, 2014, DOI: 10.3109/0284186X.2014.925578

[22] Georg D, Knöös T, McClean, Current status and future perspective of flattening filter free photon beams, Med. Phys, Vol 38 (8), 1280-1293, 2011, DOI: 10.1118/1.3554643

[23] Ghasemi F, Davani F, Rashti M, Abbasi M, Implementation of Main Waveguide Cavities of Electron Linear Accelerator Using Integrated and Separable Methods and Comparing Their Performance, International Journal of Electromagnetics and Applications, Vol 2 (6), 163-168, 2012, DOI: 10.5923/j.ijea.20120206.05

[24] Giraud P, Houle A, Respiratory Gating for Radiotherapy: Main Technical Aspects and Clinical Benefits, ISRN Pulmonology, Vol 2013, 2013, DOI: 10.1155/2013/519602

[25] Henríquez F, Castrillón S, "A quality index for equivalent uniform dose", J Med Phys, Vol 36 (3), 126âĂŞ132, 2011, DOI: 10.4103/0971-6203.83466

[26] Hrbacek J, Lang S, Graydon S, Klöck S, Riesterer O, Dosimetric comparison of flattened and unflattened beams for stereotactic ablative radiotherapy of stage I non-small cell lung cancer, Med Phys, Vol 41 (3), 2014, DOI: 10.1118/1.4866231

[27] ICRU Report 50, Prescribing, Recording and Reporting Photon Beam Therapy, International Commission on Radiation Units and Measurements, 7910 Woodmanont Avenue, Bethesda, Maryland 20814, USA, 1st September 1993

[28] ICRU Report 62, Prescribing, Recording and Reporting Photon Beam Therapy (Supplement to ICRU Report 50), International Commission on Radiation Units and Measurements, 7910 Woodmanont Avenue, Bethesda, Maryland 20814, USA, 1st November 1999

[29] ICRU Report 83, Prescribing, Recording and Reporting Photon-Beam Intensity-Modulated Radiation Therapy (IMRT), The International Commission on Radiation Units and Measurements, Journal of the ICRU Vol 10 No1 (2010), DOI: 10.1093/jicru/ndq001

[30] Kostiukhina N, Sipaj A, Rollet S, Kuess P, Furtado H, Andrzejewski P, Steiner E, RauSch I, Kertész H, Georg D, Advanced Radiation Dosimetry System (ARDOS) âĂŞ A novel breathing phantom for radiation therapy, ESTRO, 2016

[31] Kostiukhina N, Sipaj A, Rollet S, Steiner E, Kuess P, Furtado H, Georg D, ARDOS Advanced Radiation Dosimetry System, Tagung der Österreichischen Gesellschaft fÃijr Medizinische Physik (ÖGMP), 2015

[32] Kragl G, Albrich D, Georg D, Radiation therapy with unflattened photon beams: Dosimetric accuracy of advanced dose calculation algorithms, Radiother Oncol., Vol 100 (3), 417-423, 2011, DOI: 10.1016/j.radonc.2011.09.001

[33] Kragl G, Baier F, Lutz S, Albrich D, Dalaryd M, Kroupa B, Wiezorek T, Knöös T, Georg D, Flattening filter free beams in SBRT and IMRT: Dosimetric assessment of peripheral doses, Z Med Phys, Vol 2, 91-101, 2011, DOI: 10.1016/j.zemedi.2010.07.003

[34] Lane D, Critical values of the Studentized Range Distribution, http://davidmlane.com/hyperstat/sr_table.html (15th August 2016)

[35] Lund-Jensen B, X-ray Imaging Laboratory, KTH, Physics Department, 1998, http://gluon.particle.kth.se/TEACHING/laboratory/xray/xray_instr.html (31st August 2016)

[36] Manual Monaco 5.00.04, Elekta, Stockholm, Sweden

[37] Marples B, Presentation: The Management of Gynecologic Cancers: Radiobiology, Beaumont Health Systems,Oakland University William Beaumont, Spring Refresher Course 2013

[38] Mayles P, Nahum A, Rosenwald J, Handbook of Radiotherapy Physics - Theory and Practice, Clatterbridge, UK Clatterbridge Centre for Oncology, U.K. Institute Curie, Paris, France, 2007, ISBN: 978-0-7503-0860-1

[39] McGrath S, Matuszak M, Yan D, Kestin L, Martinez A, Grills I, Flattening filter free beams in SBRT and IMRT: Dosimetric assessment of peripheral doses, Radiotherapy and Oncology, Vol 95, 2010, 153-157, DOI: 10.1016/j.radonc.2009.12.039

[40] Monaco 5, Comprehensive treatment planning, Elekta

[41] National Cancer Institute, http://www.cancer.gov/ (5th August 2016)

[42] National Institute of Biomedical Imaging and Bioengineering, https://www.nibib.nih.gov/science-education/science-topics/computed-tomography-ct (15th October 2016)

[43] Navarria P, Volumetric modulated arc therapy with flattening filter free (FFF) beams for stereotactic body radiation therapy (SBRT) in patients with medically inoperable early stage non small cell lung cancer (NSCLC), Radiother Oncol, Vol 107 (3), 414-418, 2013, DOI: 10.1016/j.radonc.2013.04.016

[44] Niemierko A, Reporting and analyzing dose distributions: A concept of equivalent uniform dose, Med Phys., Vol 24 (1), 103-110, 1997, DOI: 10.1118/1.598063

[45] Oesterreichische Krebshilfe Wien, https://www.krebshilfe-wien.at (27th January 2016)

[46] Omoto C, Lurquin P, Genes and DNA: A Beginner's Guide to Genetics and its Applications, Columbia University Press 2004, New York Chichester, West Sessex

[47] Ong C, Dahele M, Slotan B, Verbakel W, Dosimetric Impact of the Interplay Effect During Stereotactic Lung Radiation Therapy Delivery Using Flattening Filter-Free Beams and Volumetric Modulated Arc Therapy, Int J Radiation Oncol Biol Phys, Vol 86 (4), 743-748, 2013, DOI: 10.1016/j.ijrobp.2013.03.038

[48] Ong C, Verbakel W, Cuijpers J, Slotman B, Lagerwaard F, Senan S, Stereotactic radiotherapy for peripheral lung tumors: A comparison of volumetric modulated arc therapy with 3 other delivery techniques, Radiother Oncol, Vol 97 (3), 437-442, 2010, DOI: 10.1016/j.radonc.2010.09.027

[49] Ong C, Verbakel W, Cuijpers J, Slotman B, Senan S, Dosimetric Impact of Interplay Effect on Rapidarc Lung Stereotactic Treatment Delivery, Int J Radiat Oncol Biol Phys, Vol 79 (1), 305-311, 2011, DOI: 10.1016(j.ijrobp.2010.02.059

[50] Paddick I, A simple scoring ration to index the conformity of radiological treatment plans, J Neurosurg, 93 Suppl 3:219-222, 2000, DOI: 10.3171/jns.2000.93.supplement

[51] Papaconstadopoulos P, Hegyi G, Seuntjens J, Devic S, A protocol for EBT3 radiochromic film dosimetry using reflection scanning, Medical Physic, Vol 41, 122101, 2014, DOI: 10.1118/1.4901308

[52] Podgorsak E, Radiation Oncology Physics: A Handbook for Teachers and Students, International Atomic Energy Agency, Vienna, 2005

[53] Pyshniak V, Efficiency of biological versus physical optimization for single-arc VMAT for prostate and head and neck cases, J Appl Clin Med Phys, Vol 15 (4), 2014, DOI: 10.1120/jacmp.v15i4.4514

[54] Rauschenbach B, Mackowiak L, Malhotra H, A dosimetric comparison of three-dimensional conformal radiation, volumetric-modulated arc therapy, and dynamic conformal arc therapy in the treatment of non-small cell lung cancer using stereotactic body radiotherapy, Journal of Appplied Clincial Medical Physics, VOl 15 (4), 2014

[55] Sanne C, Einsatz von radiochromen Filmen zur dosimetrischen Verifikarion von speziellen radiotherapeutischen Anwednung, Masterarbeit, Heinrich Heine Universität Düsseldorf, 2010

[56] Scarfe W, Farman Allan, What is Cone-Beam CT and How Does it Work?, The Dental Clinics of North America, Vol 52, 707-790, 2008, DOI: 10.1016/j.cden.2008.05.005

[57] Sloman B, Elekta, Treatment Planning Tips and Tricks using Monaco 5.1

[58] Spektrum Akademischer Verlag, Heidelberg, 1988, http://www.spektrum.de/lexikon/physik/betatron/1485, (31st August 2016)

[59] Statistik Austria, Österreichisches Krebsregister, Erstellt am 14.10.2015. Luftröhre, Bronchien und Lunge (C33-C34) - Krebsinzidenz (Neuerkrankungen pro Jahr), Österreich ab 1983

[60] Statistik Austria, Österreichische Todesursachenstatistik, Erstellt am 14.10.2015. Luftröhre, Bronchien und Lunge (C33-C34) - Krebsmortalität (Sterbefälle pro Jahr), Österreich ab 1983

[61] Styf E, Intensity modulated radiotherapy (IMRT) in head and neck cancer: A comparative treatment planning study using physically and biologically based optimization, Umeå University, Department of Radiation Science, Radiation Physics, SE-90187 Umeå, Sweden, 2008

[62] The University of Western Australia, School of Physics, Dynamic Conformal Arc Therapy in Stereotactic Ablative Radiotherapy, http://www.physics.uwa.edu.au/research/medical-radiation/projects/dcat-sabr (26th January 2016))

[63] Tyler M, Quantification of interplay and gradient effects for lung stereotactic ablative radiotherapy (SABR) treatments, J Appl Clin Med Phys, Vol 17 (1), 158-166, 2016

[64] Valdagni R, Rancati T, Reducing rectal injury during external beam radiotherapy for prostate cancer, Nat Rev Urol, Vol 10 (6), 345-357, 2013, DOI: 10.1038/nrurol.2013.96

[65] Vassiliev O, Kry S, Chang J, Balter P, Titt U, Mohan R, Stereotactic radiotherapy for lung cancer using a flattening filter free Clinac, Journal of Applied Clinical Medical Physics, Vol 10 (1), 2009, DOI: 10.1120/jacmp.v10i1.2880

[66] Vassiliev O, Titt W, Pönisch F, Kry S, Mohan R, Gillin M, Dosimetric properties of photon beams from a flattening filter free clincial accelerator, Phys Med Biol, Vol 51, 1907 - 1917, 2006, DOI: 10.1088/0031-9155/51/7/019

[67] Wennerstrom C, SBRT Lung Planning Tips and Tricks: VMAT vs. Dynamic Conformal Arc, Department of Radiation Oncology and Gamma Knife, Kettering Medical Center, Ohio

[68] Wu Q, Mohan R, Niemierko A, Schmidt-Ullrich R, Optimization of intensity-modulated radiotherapy plans based on the equivalent uniform dose, Int J Radiation Oncology Biol Phys, Vol 52 (1), 224-235, 2002

[69] Zhang G, Ku L, Dilling T, Stevens C, Zhang R, Li W, Feygelman V, Volumetric modulated arc planning for lung stereotactic body radiotherapy using conventinal and unflattened photon beams: a dosimetric comparison with 3D technique, Radiat Oncol, Vol 6, 2001, DOI: 10.1186/1748-717X-6-152

[70] Zhang J, Lu J, Hong D, Ma C, Pend X, Lin Z, A dosimetric and treatment efficiency evaluation of stereotactic body radiation therapy for peripheral lung cancer using flattening filter free beams, Oncotarget, 2016, DOI:10.18632/oncotarget.12071

[71] Zink K., Einführung in die Strahlentherapie und Therapie mit offenen Nukliden (Stand: Sommersemester 2004), Fachhochschule Gießen-Friedberg, Fachbereich KMUB, Gießen, Deutschland